Localized In-Situ Density Measurement in Low Earth Orbit via Drag Torque Estimation

Localized In-Situ Density Measurement in Low Earth Orbit via Drag Torque Estimation

Riley M. Fitzgerald* and Kerri L. Cahoy†
Massachusetts Institute of Technology, Cambridge, MA, 02139

Orbital forecasting is a chief driver of precision satellite operations. The largest contributor to orbital propagation error in low orbits is atmospheric drag, which varies widely due to altitude, latitude, and solar activity. Accurate in-situ measurements would enable improved orbital forecasting, but conventional methods for density measurement require precision accelerometers, tracking systems, or processing on the ground.

This work introduces the novel Satellite Producing Aerodynamic Torque to Understand LEO Atmosphere (SPATULA) concept, and provides supporting preliminary simulations of (1) the density recovery capability of a SPATULA satellite, and (2) the efficacy of estimating a global density map via a SPATULA constellation.

Results suggest that a SPATULA CubeSat could provide measurement capability on a par with current methods in both error and bandwidth using commercially-available sensors. This measurement is enabled by considering drag torque instead of drag force; measuring in this domain eliminates many sources of perturbation, and leverages the large body of preexisting attitude sensors for small satellites to achieve a density measurement with RMS error of 1×10^{-13} kg/m^3 and bandwidth of 1 min^{-1}. The high accuracy and low expected cost of this method would enable a constellation to estimate a high-order spherical harmonic global density map in real time.

*Doctoral Student, MIT department of Aeronautics and Astronautics.
†Associate Professor, MIT department of Aeronautics and Astronautics. Associate Fellow AIAA.

Nomenclature

$\mu_\oplus$	=	Earth gravitational parameter
P	=	Orbital period
Π	=	True longitude from X axis
J	=	Moment of Inertia
ρ	=	Atmospheric density
C_D	=	Drag coefficient of the satellite
$\mathbf{r}$	=	Position vector
$\mathbf{v}$	=	Velocity vector
θ	=	Angle of craft w.r.t. the X axis
ω_{rw}	=	Reaction wheel rate
τ	=	Torque about Z axis
$\mathcal{N}$	=	Gaussian (normal) Random Variable
σ	=	Standard deviation of a Gaussian
Δ	=	Quantization resolution
f_s	=	Sample frequency in Hz
ω	=	Bandwidth in rad/s
$\mathcal{B}$	=	Bias of a sensor
$\Delta\mathcal{B}$	=	Bias instability of a sensor
k	=	Scalar gain
s	=	Laplace domain complex frequency
$Y_{\ell,m}$	=	Spherical harmonic of degree ℓ, order m
$\dot{\square}$	=	Time derivative of some variable $\square$
$\square'$	=	Measurement of some variable $\square$
$\square^c$	=	Corrected version of some variable $\square$
$\hat{\square}$	=	Estimate of some variable $\square$
$\bar{\square}$	=	Mean of some variable $\square$

I. Introduction

As the current push towards the commercialization of space expands the utilization of low Earth orbit (LEO) by satellites, accurate orbital forecasting is becoming increasingly important. More and more small satellites are seeking to use this space, and their positions and orbits need to be tracked or predicted with better accuracy in order to ensure safe usage of this space. As commercial constellations of hundreds or thousands of small satellites in LEO become common [1], accurate prediction of LEO perturbations will become necessary to ensure proper orbital management in the long term.

In LEO, the perturbations with the largest effect on propagators are the J_2 effects caused by non-sphericity of the Earth, closely followed by atmospheric drag, and then other third-body effects and gravity potential terms [2]. However, gravitational effects, though complex, are predictable based on the position of the satellite and third bodies. Thus, the greatest errors in real-life orbit prediction often come from the uncertainties of atmospheric drag effects. Though there

are many models used to predict these, often to great precision [2], accurate real-time measurements could provide better input to orbit propagators and provide the basis of new, improved thermospheric models, as well as decrease the error induced in orbital propagation by unpredictable weather and space weather events. Solar particle events, solar flares, and the solar cycle greatly affect the overall atmospheric density in LEO, and dynamics such as tides and waves within the atmosphere can cause further local deviation from expected values. However, these measurements are very difficult to make, especially in-situ, due to the very low densities being measured. High-vacuum gauges often couple the measurement with gas temperature, also very difficult to predict in the free-molecular flow region considered. A common solution is to measure the density through its force, and its effect on satellite orbits. Given the incredibly low densities, on the order of grams per kilometer cubed, it is effective to increase the measured quantity by taking advantage of the high orbital velocity to produce a drag force orders of magnitude higher than the density alone. However, taking these measurements in real time is difficult due to the number of perturbing forces with a greater effect than that of drag. Figure 1(a) shows the worst-case magnitudes of the different perturbation forces and torques in LEO, as normalized to the effects of drag. In Fig. 1 it can clearly be seen that the drag force can be overwhelmed by gravitational potential terms and third-body effects, and could be lost without proper compensation and prediction.

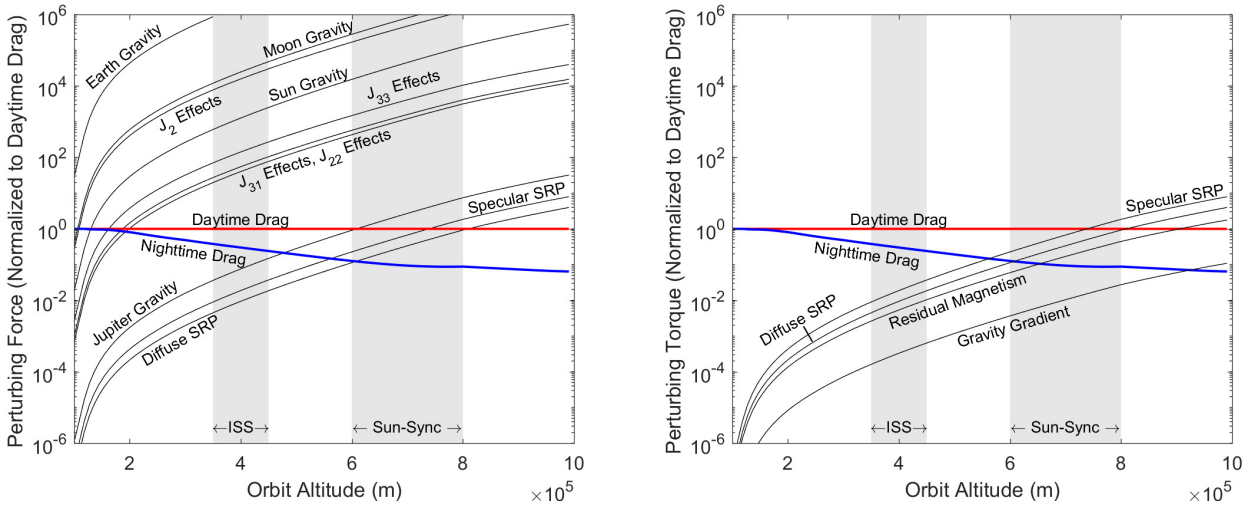

Fig. 1 The relative magnitudes of perturbing forces (left) and torques (right) experienced by a typical cubesat in LEO. Values have been normalized by the maximum effect of drag at that altitude, as calculated by the Harris-Priester atmospheric model [3]. All perturbations were evaluated in the worst case. Note how perturbing forces are dominant over the drag force in common LEO orbits, but drag is clearly the dominant torque in LEO.

Figure 1(b), however, shows the magnitudes or perturbing torques relative to those induced by drag. It can be seen that most of the perturbing force terms are due to distant or weak gravity fields, and so do not induce appreciable torques. (Their gravity gradient torque would be far less than that of Earth, which is the weakest torque shown for here.) Real-time measurement of drag effects, then, may be best enabled by measuring them in the torque domain.

The increased availability and decreased cost of small satellite buses, sensors, and launches could decrease costs

and enable the measurement of atmospheric density effects around the globe in real time. The goal of this work is to demonstrate the feasibility of performing high-bandwidth measurement of drag torque effects on a cubesat using readily-available cubesat sensors, in order to enable a constellation of small, inexpensive satellites to map the LEO atmospheric density around the globe in real time.

II. Background

A. Acceleration-Measuring Satellites

1. DANDE

There is a history of trying to measure atmospheric density through in-situ satellites. The most recent example is the Drag And Neutral Density Explorer (DANDE) satellite proposed by the Colorado Space Grant Consortium and University of Colorado at Boulder [4]. The goal of this satellite was to produce in-situ density measurements in the LEO region around 350 km altitude. DANDE was a 50 kg spherical satellite,which aimed to use six high-precision accelerometers to measure the deceleration caused by drag directly. Due to the large size of the accelerometer system, these measurements would not have been able to be performed by a cubesat-class satellite. Unfortunately, the DANDE spacecraft experienced an on-orbit control malfunction, and no data was recovered, so the in-situ performance cannot be analyzed, but the planned performance can be examined.

The accelerometer-based measurement was to have a horizontal resolution of 500 km, or about 64 s of along-track time [5]. This approximately 60-second temporal resolution was set by the cadence of the accelerometer output, and sets a good baseline for comparison to SPATULA. The overall error of the system was predicted to be approximately 2×10^{-12} kg/m^3, accounting for changing cross sectional area, winds, and drag coefficients.

2. CHAMP and GRACE

The Challenging Minisatellite Payload (CHAMP) and Gravity Recovery And Climate Experiment (GRACE) are similar satellites, and each carries a high-precision accelerometer, the STAR (Space Three-axis Accelerometer for Research) and SuperSTAR respectively. Both have enabled measurement of atmospheric density to high accuracy, once the accelerometer data has been calibrated and processed on the ground. The STAR data from CHAMP has been shown to be sufficient to map the global density distribution over the course of a day, since its acceleration measurement has a precision of approximately 1×10^{-9} g [6]. Other sources of acceleration must be modeled and subtracted, but the resulting density data is able to follow predictive models within a few percent error when available, and show complex polar transients not predicted by the model [6]. The CHAMP satellite is also able to measure atmospheric density though radio occultation [7], but this measurement technique can only sense neutral density up to 60-80 km in altitude, far under the normal operating range of LEO satellites.

The GRACE satellites are similar in design, but have the primary mission of measuring the gravitational potential field of the Earth, accomplished by microwave ranging between the two satellites. The variations in this range allow the satellites to reconstruct the gravity potential field of the Earth. However, the highly sensitive system is also able to pick up forces from the variation of density in the upper atmosphere [8]. The GRACE satellites are able to use their onboard high-precision SuperSTAR accelerometers to estimate the non-gravitational forces to high accuracy. The data produced by these accelerometers is offloaded to the ground, where it is processed along with the gravitational data to produce a measurement of the drag force. The accelerometers are able to measure at 3 Hz with a listed acceleration precision of 1×10^{-12} g [8]. This measurement is extremely precise, but is subject to noise forces that must be calibrated out on the ground. When analyzed, the data shows close tracking with a density profile from 5×10^{-13} kg/m^3 to 3×10^{-12} kg/m^3, showing quick transient deviations from predicted models.

The performance of these systems is excellent, but the high-precision accelerometers used are very specialized, expensive instruments unsuited for small satellite use, and the data must be processed on the ground to yield useful estimates. SPATULA aims to produce measurements of similar quality, but estimated on-board and performed by a cubesat with commercially-available sensors.

B. Other Methods of Density Measurement

1. High-Vacuum Gauges

Measurement of the drag force is not the only way to measure the density in LEO. Many vacuum gauge technologies have been developed that are capable of detecting the pressures in LEO. For example, Tighe et al. [9] have demonstrated a cold-cathode discharge vacuum gauge on orbit. The gauge is on the ram face of the Columbus Laboratory on the ISS. This gauge is easily able to measure the pressure on orbit, as well as the diurnal variation. However, this pressure data cannot be simply converted directly into density measurements. The instrument shows a strong dependence on attitude, experiencing a difference of multiple orders of magnitude when the station reoriented to face the instrument in the anti-ram direction. Additionally, the diurnal pressure variation is not just a function of density change; pressure is coupled with temperature variation caused by solar heating. These effects, combined with the large size and expense of the precision gauge, make this type of measurement unsuitable for low-cost small satellite missions.

2. Constellation Communication

Carefully-controlled communication between satellites in orbit can provide another way to measure the drag effects, by allowing precise measurement of the positions of satellites relative to each other. GPS is the most common method of obtaining these measurements, and provides a simple, standardized way to measure the position and velocity of a spacecraft. Using this data, it is theoretically possible to back out the effects of drag on a satellite. However, because the forces involved are so small relative to the GPS noise, it is difficult in practice to read anything finer than an

orbit-averaged density from GPS data [10].

A self-referential constellation could provide better density tracking information. It has been shown by Hinks and Psiaki [11] that a constellation of 50-100 satellites in multiple orbital planes could well estimate the atmospheric density using ranging crosslinks with cm-scale accuracy to produce a set of cross-constellation ranges, which can then be observed to note high-drag areas. The model requires some prior knowledge about the density in order to manage estimate error, but has been shown to be able to reduce uncertainty in known measurements as well as to increase the fidelity of the constellation's own orbit propagation. This shows the value of a constellation in measuring density, but also emphasizes the need for the satellites involved to be low-cost, due to the large number of required satellites.

3. Passive Body Tracking

The ground tracking of passive bodies is a proven method for the analysis of orbital perturbations, including drag. The technique has been used even as far away as Mars; radio tracking data of the Mars Odyssey and Mars Reconnaissance Orbiter aerobraking and orbital decay have allowed for the probing of the Martian atmosphere [12].

The advantage of ground-based tracking is that the object tracked need not have any expensive measurement equipment, or even be operational. This means that simple, cheap objects with well-characterized areas and drag coefficients can be used. Orbital Debris Radar Calibration Spheres (ODERACS), Starshine spheres, Calspheres, GFZ-1, and Taifun calibration spheres are all small spherical bodies used by ground tracking stations to calibrate radar and measure orbital decay [13]. These spheres are made to be tracked either by radar (ODERACS, etc.) or by optical instruments (Starshine). The position and velocity measurement of these spheres can provide good estimations for the local density, as well as enable the study of coefficients of drag because of their well-known physical properties. Their deorbit patterns especially have enabled study of drag coefficients [13].

Radar (or optical) tracking of passive bodies can reconstruct an atmospheric density model well, even if the bandwidth or resolution of the measurements is unable to capture small variations in the density. It has been shown by Shoemaker et al. [14] that tomographic methods can be used to reconstruct density features beyond the resolution of any one measurement by considering different measurements as slices. By measuring the effect on many different satellites as they pass through a given region with different orbital properties, it is possible to reconstruct a fine density map of the region. Measurements produced using this method are spatially fine, but are necessarily time-averaged: good for producing atmospheric models, but bad for real-time orbit propagation.

C. Contribution

It can be seen that there is a need for a density measurement platform that is simultaneously high-resolution, real-time, and low-cost. To address this need, this work proposes a novel method of in-situ density measurement, the Satellite Producing Aerodynamic Torque to Understand LEO Atmosphere (SPATULA). Preliminary simulations of both

single SPATULA satellites and a constellation of SPATULAs are performed to show that (1) by measuring atmospheric drag force through its contribution to external torque, it is possible to provide atmospheric density estimates with accuracy and bandwidth comparable to other modern methods, but do so in real-time in a cubesat form factor with commercially-available components and sensors; and (2) a constellation of such satellites would be able to recover a global density map of higher order than the current state-of-the-art.

III. SPATULA Spacecraft, Model, and Simulation

The approach used is to numerically simulate a small cubesat attitude control system in orbit to assess the viability of measuring drag effects through torque. Perturbing forces and torques are simulated, as well as the noisy sensor readings. These readings are then run though a series of controllers and estimators in order to extract a measurement of the torque, and ultimately density, experienced by the craft.

A. SPATULA Concept of Operations and Spacecraft Model

The proposed spacecraft concept is the Satellite Producing Aerodynamic Torque to Understand LEO Atmosphere, or SPATULA. Figure 2 shows the overall concept: The satellite is aerodynamically-unbalanced by means of a drag flap extended along the local vertical, perpendicular to the orbital velocity. This induces a drag torque which can be estimated via attitude sensors to infer the density. When the accumulated angular momentum builds up and approaches reaction wheel saturation, the satellite pauses the estimation and flips around, allowing the drag torque to act in the opposite direction. The estimation then continues while the drag torque desaturates the reaction wheels, and the process repeats. (The logic of the desaturation flip is treated with greater detail in Section III.C.)

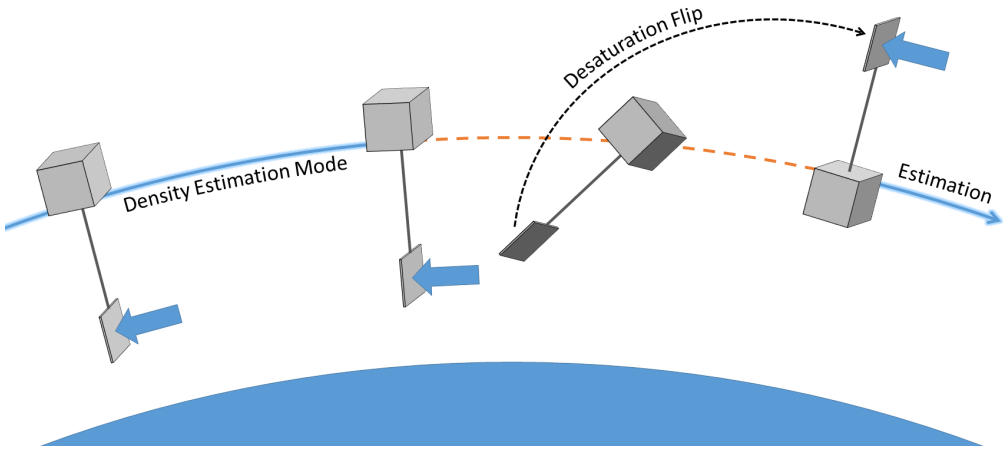

Fig. 2 The SPATULA Concept of Operations

The modeled SPATULA is built on a 1U (10 cm × 10 cm × 10 cm) cubesat bus, with a deployable drag flap. The drag flap consists of a 10 cm × 10 cm drag panel at the end of a deployable arm. The overall structure of the craft is

shown in Fig. 3.

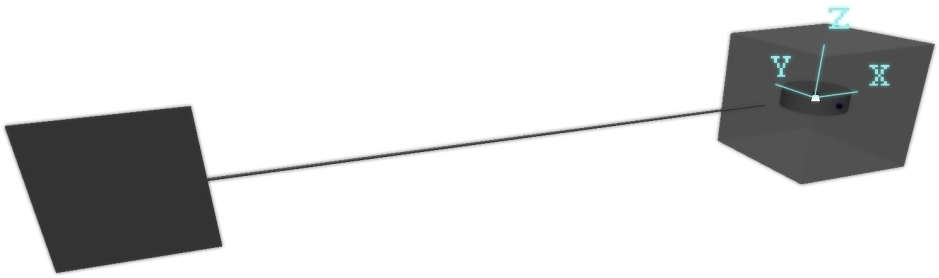

Fig. 3 The modeled SPATULA Spacecraft, as simulated by Simulink SimMechanics. In the displayed coordinate frame, X is the local vertical, Y is along the velocity vector, and Z is normal to the orbital plane.

The model SPATULA spacecraft was simulated using Simulink SimMechanics. The spacecraft was treated as a rigid body, since the perturbing torques considered were small and of low frequency. Three spacecraft degrees of freedom were considered: the (X,Y) position in the orbital plane, and the angle of rotation θ about the Z axis normal to the orbital plane. (This coordinate frame is shown in Fig. 3.) This is reasonable, since the symmetry of the spacecraft about the X-Y plane minimizes torques induced in the plane, and out-of plane orbital forces like those due to J_2 effects induce minimal torques. The spacecraft's orbit was simulated as a circular equatorial orbit at an altitude of 400 km. (The circular orbit is typical of operations, but the altitude could vary based on desired measurement location.) All attitude dynamics and orbital dynamics were modeled numerically by the SimMechanics Multibody physics solvers, running variable-step algorithms with a relative tolerance of 1×10^{-6}. Table 1 lists the key physical parameters of the modeled SPATULA spacecraft.

Table 1 Key Physical Parameters of the SPATULA Spacecraft

Spacecraft Parameter	Symbol	Value	Notes
Reaction Wheel Mass	m_{rw}	0.050 kg	—
Reaction Wheel MOI	J_{rw}	2.8×10^{-5} kgm^2	—
Spacecraft Body Mass	m_{body}	1.0 kg	Not including reaction wheel
Spacecraft Body MOI	J_{body}	3.0×10^{-3} kgm^2	Not including reaction wheel
Body Cube Dimension	d_{body}	10 cm	Cubesat standard body size
Flap Dimension	d_{flap}	10 cm	—
Flap Thickness	t_{flap}	1.0 mm	—
Flap Mass	m_{flap}	.010 kg	—
Drag Arm Length	L_{arm}	0.525 m	From body center to flap center
Drag Arm Diameter	D_{arm}	2.0 mm	—
Drag Arm Mass	m_{arm}	0.031 kg	—

All physical values were chosen to reflect realistic materials and properties, as well as typical masses for these components (where available). The length of the drag arm was chosen to optimize the angular acceleration given a

fixed Moment of Inertia (MOI) for both the body and the flap itself. Since torque is proportional to the moment arm, but moment of inertia increases with the square of the length, there is a maximum value of angular acceleration as a function of arm length for L_{arm} = 0.525 m, as can be seen in Fig. 4.

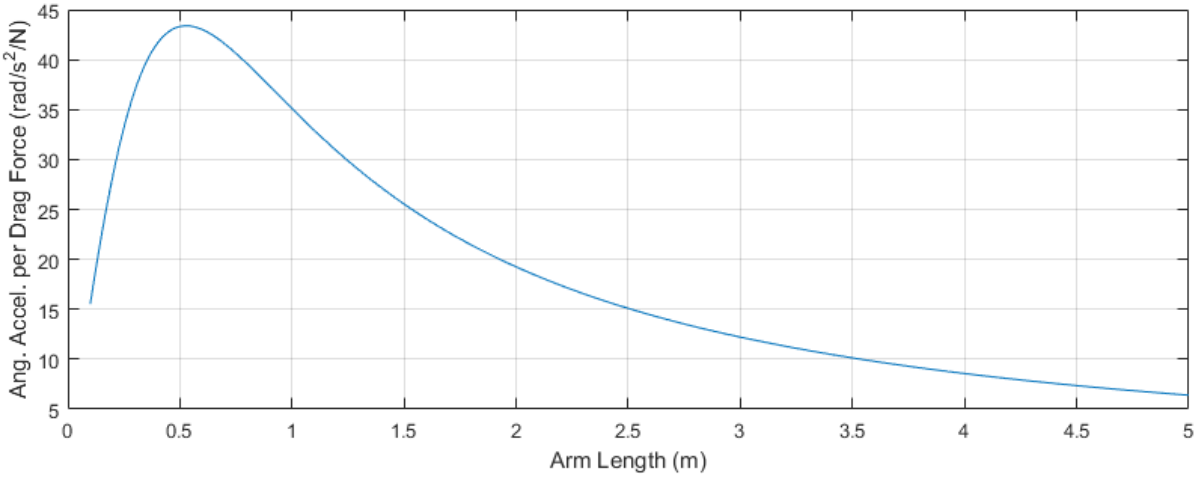

Fig. 4 The optimization of the arm length to maximize angular acceleration

Table 2 lists the modeled sensors, approximate real-world equivalents, data outputs, and noise parameters. σ is the standard deviation of white noise, Δ is the discretization resolution, and f_s is the sampling frequency. $\Delta\mathcal{B}$ is the bias instability of the gyroscope. The primes on the outputs indicate noisy measurements of the indicated variable. More details on the sensor models used are given in the Appendix.

Table 2 Sensor Model Noise and Discretization Parameters

Sensor Model	Derived From	Output	1σ	Δ	f_s	$\Delta\mathcal{B}$
Star Tracker	NST-1 [15]	θ'_{st}	2.33"	1"	10 Hz	—
Horizon Sensor	MAI-SES [16]	θ'_{eh}	0.25°	.01°	1000 Hz	—
MEMS Gyroscope	ADIS16334 [17]	$\dot{\theta}'_{gy}$	0.19°/s	0.0125°/s	1000 Hz	0.0072°/s
RW Rate Sensor	—	ω'_{rw}	5°/s	5°/s	1000 Hz	—
GPS (Position)	piNAV-L1 [18]	$\boldsymbol{r}'_{gps}$	5 m	1 mm	1 Hz	—
GPS (Velocity)	piNAV-L1 [18]	$\boldsymbol{v}'_{gps}$	0.05 m/s	1 mm/s	1 Hz	—

The simulation includes spherical-Earth gravity and gravity gradient torque; specular, diffuse, and absorbed solar radiation pressure; atmospheric drag force and torque; and finite-bandwidth reaction wheel dynamics. Again, the details of the force, torque, and actuator models are provided in the Appendix.

B. Calibration Maneuver

Because SPATULA aims to measure very small torques, the first thing the simulated SPATULA spacecraft does upon deploying its drag flap is to recalibrate its knowledge of its own moment of inertia J_{sat}. The easiest and most

effective way to do this is to study the motion of the spacecraft under a known torque.

The reaction wheel modeled can store a total of 0.018 Nms of angular momentum [19], equivalent to an 18-second burst of the maximum command torque. To work with margin, the calibration maneuver thus consists of two 15-second bursts of a constant 80% maximum torque in opposite directions. This leaves the spacecraft with the same stored momentum as at the beginning of the maneuver, while still providing long-duration constant-torque inputs for the measurement of moment of inertia. Figure 5 shows the calibration torque profile and response.

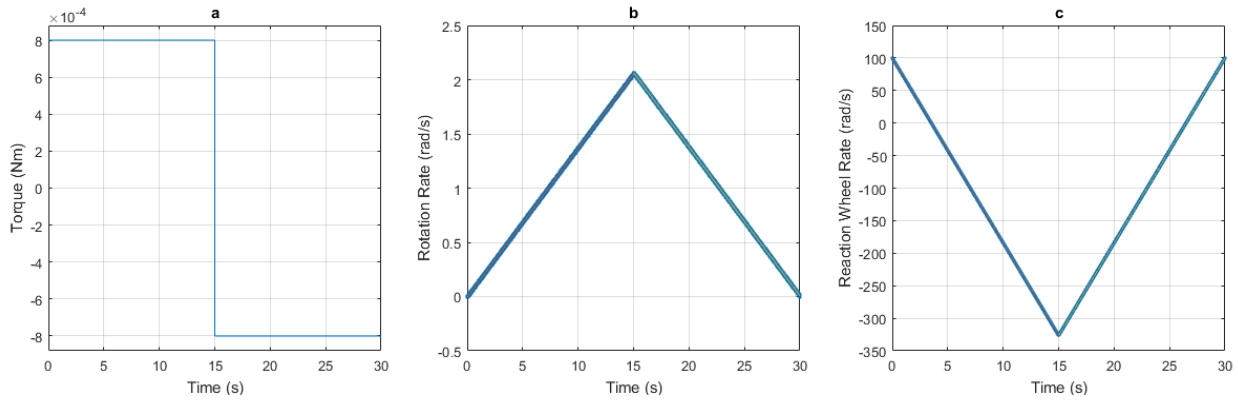

Fig. 5 The calibration pattern used to identify the system moment of inertia. a) The torque profile provided by the reaction wheel. b) The angular rate response of the spacecraft. c) The angular rate response of the reaction wheel.

The raw gyroscope data and the raw reaction wheel rate data is processed to measure the moment of inertia of the satellite and the reaction wheel. Two lines of best fit are calculated though the two phases of the noisy gyroscope data, and the average slope of these two lines, $\bar{\dot{\theta}}$, is used to calculate the estimated satellite moment of inertia J_{sat} from the calibration torque command τ_{cal} through Equation 1. Similarly, the raw reaction wheel rate data is fit with two lines of average slope $\bar{\dot{\omega}}_{rw}$ used to calculate the reaction wheel moment of inertia J_{rw} by Equation 2.

$$J_{sat} = \frac{\tau_{cal}}{\bar{\ddot{\theta}}} \tag{1}$$

$$J_{rw} = -\frac{\tau_{cal}}{\bar{\dot{\omega}}_{rw}} \tag{2}$$

In the considered one-axis model, this maneuver is sufficient to characterize the spacecraft moment of inertia about the measurement axis. In a full-fidelity model or real implementation a single maneuver like this would only be able to estimate one principle component of the inertia matrix; a more complex maneuver and estimation method, such as those developed by Norman, Peckt, and O'Shaughnessy [20], would be needed to estimate the entire matrix.

C. Measurement Mode Control Methodology

Control of the spacecraft is accomplished by a simple LQR controller, derived in ignorance of reaction wheel dynamics or external torques. For the derivation of the controller, the spacecraft is assumed to obey dynamics given by

$$\begin{bmatrix}\dot{\theta}\\ \ddot{\theta}\end{bmatrix} = \begin{bmatrix}0 & 1\\ 0 & 0\end{bmatrix}\begin{bmatrix}\theta\\ \dot{\theta}\end{bmatrix} + \begin{bmatrix}0\\ J_{sat}^{-1}\end{bmatrix}\tau_c\,. \tag{3}$$

Controller costs were chosen by Bryson's rule [21], with approximate maximum angular error of 0.03 rad, maximum angular rate error 0.003 rad/s, and maximum control torque 1 mNm specified by the reaction wheel. The resulting controller cost matrices are

$$Q_c = \begin{bmatrix}0.1 & 0\\ 0 & 10\end{bmatrix}, \tag{4}$$

$$R_c = [1000]\,. \tag{5}$$

Solving for the LQR gain specified by these costs and the system matrices using the MatLab `lqr` solver, the optimal controller gain K is found to be of the form

$$\tau_c = \underbrace{\begin{bmatrix}0.01 & 0.1\end{bmatrix}}_{K}(\boldsymbol{x}_c - \hat{\boldsymbol{x}})\,. \tag{6}$$

The commanded state $\boldsymbol{x}_c$ is defined by the nadir-pointing angular position, calculated as the estimated true longitude of the orbit $\hat{\Pi}(t) = \tan^{-1}(\hat{Y}/\hat{X})$, and the estimated orbital mean motion $\hat{n} = \sqrt{\mu_\oplus/\hat{r}^3}$. However, it must be considered that positioning the drag flap on the same side of the craft for extended periods will induce a momentum buildup in the main reaction wheel. This can be countered by rotating the craft 180°about the Z axis to place the drag flap on the anti-nadir side of the craft once the reaction wheel has stored a predetermined amount of momentum, specified by a reaction wheel rate ω_{flip}. The desaturation mode of the craft is captured by the variable *desat*, which ranges from zero to one as the craft flips about the considered axis according to the control logic summarized in Fig. 6.

$$\boldsymbol{x}_c = \begin{bmatrix}\hat{\Pi}(t) + \pi\,\text{desat}\\ \sqrt{\mu_\oplus/\hat{r}^3}\end{bmatrix} \tag{7}$$

$$\text{desat} \in [0, 1] \tag{8}$$

Additionally, the output of all estimators is paused for two minutes at the initiation of a desaturation flip maneuver in order to prevent noise from throwing off the measurement. The external torque estimate and external torque estimate mean are both multiplied by -1 at the end of this pause period before resuming, to capture the fact that the torque is now equal in magnitude but acting in the opposite direction.

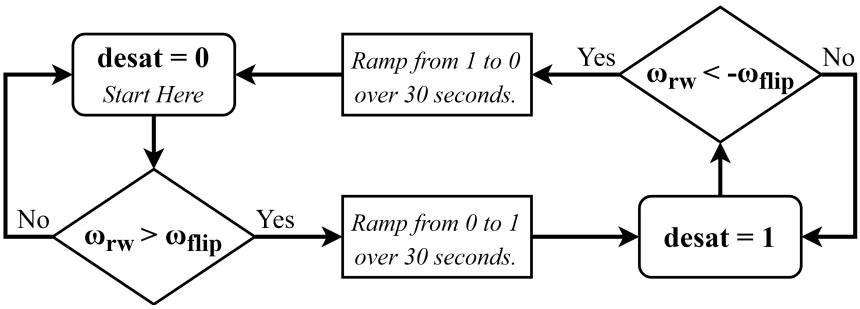

Fig. 6 The logic followed by the nadir state command x_c in setting variable *desat*.

D. Measurement Mode Estimation Methodology

1. Gyroscope Bias Correction

In order to sense the small, low-frequency changes in angular momentum caused by the external torques, it is necessary to account for the bias instability of the MEMS gyroscope. Extracting the bias information from the gyroscope output requires referencing the output against another measurement of angular rate. Since the bias drift is slow, the rate baseline measurement can also be slow. In this case, the best available measurement of rate is from the change of the star tracker reading over time. The current bias estimate $\hat{\mathcal{B}}(t)$ is estimated by applying first-order low-pass filter transfer function to the incoming gyro signal, a derivative and first-order low-pass transfer function to the star tracker signal, and taking the difference.

$$\hat{\mathcal{B}}(t) = \mathcal{L}^{-1}\left\{\frac{1}{s/\omega_{\mathcal{B}}+1}\dot{\Theta}'_{gy} - \frac{s}{s/\omega_{\mathcal{B}}+1}\Theta'_{st}\right\} \tag{9}$$

$\dot{\Theta}'_{gy}$ indicates the angular rate signal of the gyroscope considered in the Laplace domain, and Θ'_{st} indicates the angular position signal from the star tracker considered in the Laplace domain, where both are converted to continuous-time signals via zero-order-holds. The bandwidth of the bias correction $\omega_{\mathcal{B}}$ was chosen as $\frac{2\pi}{100}$ because the bias instability drift is known to have a characteristic time of 100 s. Thus, transients and noise quicker than this are rejected by the filters, and the bias is given by the low-frequency difference between the filtered gyroscope rate and the average rate seen by the star tracker. This bias is then subtracted from the gyroscope signal to yield a corrected gyroscope measurement $\dot{\theta}'^{c}_{gy}(t)$ before being fed to the attitude estimation filter.

2. Attitude State Estimation

Attitude state estimation is performed by a continuous-time Kalman filter, or Linear-Quadratic Estimator (LQE). The state $\boldsymbol{x}$ is composed of the angular position, angular rate, reaction wheel rate, and current reaction wheel torque. The measurement vector $\boldsymbol{y}$ is composed of the measurements from the corrected star tracker, earth horizon sensor, corrected gyroscope, and reaction wheel rate sensor, all considered as continuous-time signals by zero-order holds. The correction of the star tracker involves only adding a constant equal to the expected angular drift (the orbital mean

motion n) over half the sample period of the star tracker, or $\frac{1}{2}n/f_{s,st}$. This corrects the signal so that the average value of the continuous-time signal over the zero-order hold gives the correct value, and is necessary only because of the high accuracy and low sample rate of the sensor. The input to the system $\boldsymbol{u}$ is composed of the commanded reaction wheel torque τ_c and the mean external torque $\bar{\tau}_{ex}$, the second of which acts only to enhance the fidelity of state prediction.

$$\boldsymbol{x} = \begin{bmatrix} \theta & \dot{\theta} & \omega_{rw} & \tau_{rw} \end{bmatrix}^T \tag{10}$$

$$\boldsymbol{y} = \begin{bmatrix} \theta'^c_{st} & \theta'_{eh} & \dot{\theta}'^c_{gy} & \omega'_{rw} \end{bmatrix}^T \tag{11}$$

$$\boldsymbol{u} = \begin{bmatrix} \tau_c & \bar{\tau}_{ex} \end{bmatrix}^T \tag{12}$$

For the purposes of the Kalman filter, the state is assumed to evolve according to the dynamics of Equation 13, which defines the state matrix A and input matrix B of the state-space system.

$$\dot{\boldsymbol{x}} = \frac{\mathrm{d}}{\mathrm{d}t}\begin{bmatrix} \theta \\ \dot{\theta} \\ \omega_{rw} \\ \tau_{rw} \end{bmatrix} = \begin{bmatrix} \dot{\theta} \\ \tau_{rw}/J_{sat} + \bar{\tau}_{ex} \\ -\tau_{rw}/J_{rw} \\ k_{rw}\left(\tau_c - \tau_{rw}\right) \end{bmatrix} = \underbrace{\begin{bmatrix} 0 & 1 & 0 & 0 \\ 0 & 0 & 0 & J_{sat}^{-1} \\ 0 & 0 & 0 & -J_{rw}^{-1} \\ 0 & 0 & 0 & -k_{rw} \end{bmatrix}}_{A} \boldsymbol{x} + \underbrace{\begin{bmatrix} 0 & 0 \\ 0 & J_{sat}^{-1} \\ 0 & 0 \\ k_{rw} & 0 \end{bmatrix}}_{B} \boldsymbol{u} \tag{13}$$

The measurement matrix C is defined by which states of x go to which of the four sensors. The star tracker and earth horizon sensor both examine $\theta' \approx x_1$ directly, the corrected gyroscope examines $\dot{\theta}' \approx x_2$ directly, and the reaction wheel sensor measures the reaction wheel rate with respect to the rotating craft body, or $\omega'_{rw} \approx x_3 - x_2$. Therefore, the measurement matrix C and feedthrough matrix D are given by

$$\boldsymbol{y} = \underbrace{\begin{bmatrix} 1 & 0 & 0 & 0 \\ 1 & 0 & 0 & 0 \\ 0 & 1 & 0 & 0 \\ 0 & -1 & 1 & 0 \end{bmatrix}}_{C} \boldsymbol{x} + \underbrace{\mathbf{0}_{4,2}}_{D} \boldsymbol{u} \tag{14}$$

and the feedthrough matrix D is zero. The measurement noises are given by the sensor noises listed in Table 2, and define the measurement noise covariance matrix R. The process noises for each state x_i are notated as σ_{x_i}, and define the process noise covariance matrix Q. The values for each process noise term are given in Table 3, along with the

motivation for each value.

$$R = \begin{bmatrix} \sigma_{st}^2 & 0 & 0 & 0 \\ 0 & \sigma_{eh}^2 & 0 & 0 \\ 0 & 0 & \sigma_{gy}^2 & 0 \\ 0 & 0 & 0 & \sigma_{rw}^2 \end{bmatrix} \tag{15}$$

$$Q = \begin{bmatrix} \sigma_{x_1}^2 & 0 & 0 & 0 \\ 0 & \sigma_{x_2}^2 & 0 & 0 \\ 0 & 0 & \sigma_{x_3}^2 & 0 \\ 0 & 0 & 0 & \sigma_{x_4}^2 \end{bmatrix} \tag{16}$$

The matrices A, B, C, D, R, and Q are used to solve for the LQE gain matrix L using the MatLab built-in solver for Kalman filter gains, `kalman`. The LQE gain L then defines the response of the estimated state to the measurement by

$$\dot{\hat{\boldsymbol{x}}} = A\hat{\boldsymbol{x}} + B\boldsymbol{u} + \underbrace{\begin{bmatrix} 4.42 \times 10^{2} & 2.97 \times 10^{-3} & 5.78 \times 10^{-4} & -8.11 \times 10^{-7} \\ 4.84 \times 10^{1} & 3.25 \times 10^{-4} & 2.56 \times 10^{-1} & -3.58 \times 10^{-4} \\ 8.45 \times 10^{-2} & 5.68 \times 10^{-7} & 4.47 \times 10^{-4} & 6.45 \times 10^{-4} \\ 2.58 \times 10^{-9} & 1.06 \times 10^{-14} & 2.02 \times 10^{-11} & -5.91 \times 10^{-12} \end{bmatrix}}_{L} (\boldsymbol{y} - C\hat{\boldsymbol{x}}) \ . \tag{17}$$

3. External Torque Estimation

The external torque estimator takes in the estimated state $\hat{x}$ over time and uses it to estimate the external torques acting on the craft to produce the observed motion. It first produces an estimate of the angular acceleration from the estimated angular rate by applying a derivative and first-order low-pass filter transfer function with bandwidth $\omega_{\ddot{\theta}}$, the value of which is given in Table 3.

$$\hat{\ddot{\theta}}(t) = \mathcal{L}^{-1}\left\{ \frac{s}{s/\omega_{\ddot{\theta}} + 1} \hat{\dot{\Theta}} \right\} \tag{18}$$

$\hat{\dot{\Theta}}$ represents the estimate $\hat{\dot{\theta}}$ in the Laplace domain. Given this estimation of the angular acceleration, the torque that produces this angular acceleration should be $\hat{\ddot{\theta}} J_{sat}$. Subtracting from this the current estimate of reaction wheel torque gives the presumed external torque. An integrator with gain k_τ is used to produce a first measurement of the external torque, $\hat{\tau}'_{ex}$ by integrating the difference between the predicted external torque and the current primary estimate, according to the dynamics of Equation 19. The primary estimate $\hat{\tau}'_{ex}$ is then run through another low-pass filter transfer function of bandwidth ω_τ to produce the final estimate of the external torque, $\hat{\tau}_{ex}$, according to Equation 20.

$$\dot{\hat{\tau}}'_{ex} = k_\tau \left(J_{sat} \hat{\ddot{\theta}} - \hat{\tau}_{rw} - \hat{\tau}'_{ex} \right) \tag{19}$$

$$\hat{\tau}_{ex}(t) = \mathcal{L}^{-1}\left\{ \frac{1}{s/\omega_\tau + 1} \hat{\mathcal{T}}'_{ex} \right\}, \tag{20}$$

where $\hat{\mathcal{T}}'_{ex}$ is the Laplace-domain representation of $\hat{\tau}'_{ex}$. Lastly, the running external torque mean $\bar{\tau}_{ex}$ is calculated as an average of the estimated external torque over the last orbital period P (or since the simulation start if the estimator

has been running for less than an orbit). This is value is fed back to the state estimator as the second input in order to increase the fidelity of the state estimate without passing noise into the state estimate.

$$\bar{\tau}_{ex}(t) = \begin{cases} \dfrac{1}{t}\displaystyle\int_0^t \hat{\tau}_{ex}(t)\, dt & \text{if } t < P \\ \dfrac{1}{P}\displaystyle\int_{t-P}^t \hat{\tau}_{ex}(t)\, dt & \text{if } t > P \end{cases} \tag{21}$$

Table 3 Tuning Parameters and Values of the Attitude and External Torque Estimators

Estimator Parameter	Symbol	Value	Notes / Motivation
Torque Error Integrator Gain	k_τ	$2\pi/60$	Reflects 1 min^{-1} bandwidth system goal
Angular Acceleration Filter BW	$\omega_{\ddot{\theta}}$	$2\pi/12$	Tuned value necessarily faster than ω_τ
External Torque Filter BW	ω_τ	$2\pi/60$	Reflects 1 min^{-1} bandwidth system goal
Gyro Bias Correction BW	$\omega_{\mathcal{B}}$	$2\pi/100$	Reflects typical bias drift time of 100 s
θ Process Deviation	σ_{x_1}	5×10^{-3}	Tuned to reflect error in $\dot{\theta}$ estimate
$\dot{\theta}$ Process Deviation	σ_{x_2}	1×10^{-3}	Approximate max deviation of τ_{ex}/J_{sat}
ω_{rw} Process Deviation	σ_{x_3}	5×10^{-10}	Tuned, reflects predictability of ω_{rw}
τ_{rw} Process Deviation	σ_{x_4}	1×10^{-6}	Tuned, reflects uncertainty in k_{rw}

4. Position and Velocity Estimation

Since attitude estimation and effects are the main focus of this paper, a rough position and velocity estimator is used that simply assumes a given position and velocity measurement were both correct, and propagates the position according to the last known velocity vector. For GPS sample times given by t_0, t_1 ... t_n, t_{n+1} ... then the estimated position and velocity are simply given by

$$\begin{bmatrix} \hat{\mathbf{r}} \\ \hat{\mathbf{v}} \end{bmatrix}(t) = \begin{bmatrix} \mathbf{r}'_{gps} + \mathbf{v}'_{gps}(t - t_n) \\ \mathbf{v}'_{gps} \end{bmatrix}(t_n) \quad \text{for } t \in [t_n, t_{n+1}) \,. \tag{22}$$

Because the noise is low in comparison with the large position magnitudes and orbital velocities, this simple estimator is effective in providing the information necessary to extract atmospheric density. The only parameter of the position estimate that directly factors into the later estimation is the angular position of the satellite within the orbit, in order to determine the nadir direction and attitude with respect to the sun. Since the GPS has a noise standard deviation of 5 m along track, this corresponds to a (15 m)/(6771000 m) $\approx$ 0.15 arcsec of 1σ noise in the position along track, an order of magnitude under even the star tracker's resolution; the simple estimator is well justified.

5. Atmospheric Density Estimation

The last step in the chain of estimators is to try to extract the atmospheric density from the measured external torque. This is done simply by calculating the expected torques provided by the non-drag perturbations, subtracting them from the estimated external torque, and then solving for the density. A best guess for current the solar radiation pressure

torque and the gravity gradient torque are calculated from the estimated position and orientation of the spacecraft using Equations 42-48 to yield $\hat{\tau}_{SRP}$ and $\hat{\tau}_g$. These are both then run through a first-order low-pass filter transfer function identical to that filtering the external torque estimate to yeild the corrected estimates $\hat{\tau}^c_{SRP}$ and $\hat{\tau}^c_g$ in order to assure temporal consistency in the estimate. The external torque estimate is corrected to account for the desaturation logic, simply being multiplied by -1 if the flipped *desat* mode is active, yielding $\hat{\tau}^c_{ex}$. (The sign flip accounts for the fact that the external torque will be sensed in the opposite direction when the satellite flips around 180°into desaturation mode; this prevents a large jump discontinuity in measured torque when the satellite flips.) Then, the product of predicted atmospheric density and coefficient of drag is given as

$$C_D\hat{\rho}(t) = \frac{2(\hat{\tau}^c_{ex} - \hat{\tau}^c_{SRP} - \hat{\tau}^c_g)}{(A_{flap}r_{cm-flap} - A_{body}r_{cm-body})\hat{v}^2\cos(\hat{\theta} - \hat{\Pi})}. \tag{23}$$

If the coefficient of drag for the spacecraft is known, then equation 23 can be divided by C_D to give the estimated density. If not, then the system simply estimates the product of C_D and ρ.

E. Simulation Structure

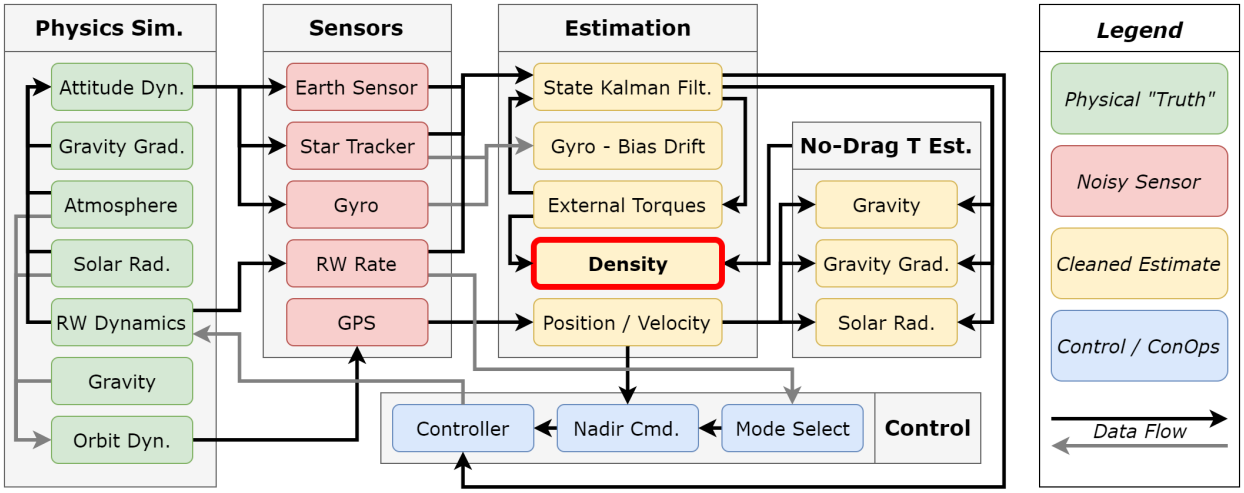

Fig. 7 The overall logic flow of the simulation. The green values represent the "physical truth" of the simulation, as modeled by SimMechanics. The red values indicate the raw noisy measurements, indicated in the math by a prime. The yellow values indicate the cleaned, estimated values, indicated in the math by a hat. The blue values represent commands.

IV. Results

A. Calibration of the Moments of Inertia

Figure 4 shows a typical response of the simulation to the calibration torque profile. Assuming that the reaction wheel torque is well-characterized and controlled as described by the RW model, a two-piece linear fit to the raw

gryroscope data produces a measurement of the moment of inertia of the satellite with approximately 0.02% error relative to the correct value. A two-piece linear fit to the raw reaction wheel data produces a measurement of the moment of inertia of the reaction wheel with an error of less than one part in one million. These estimates are more than sufficient; these errors are small compared to the noise in the system, and will be lost under other sources of measurement error. This calibration is not an appreciable source of measurement error, and for the remainder of the simulations, the estimated values for each moment of inertia are used to solve for the controller and estimator gain matrices before each run, as well as to calculate the estimated external torque.

B. MEMS Gyroscope Bias Correction

Figure 8 shows a typical gyroscope bias random walk, as well as the system's estimate of the bias. It can be seen that the high accuracy of the star tracker filtered derivative allows the system to capture even large amounts of bias drift. The maximum value of the bias drift over the course of a simulated orbit was generally on the order of 1×10^{-3} rad/s, which corresponds to approximately 90% of the rotational rate of the satellite. The SPATULA density estimator would be unable to function over the course of the orbit without the corrections provided by the bias corrector.

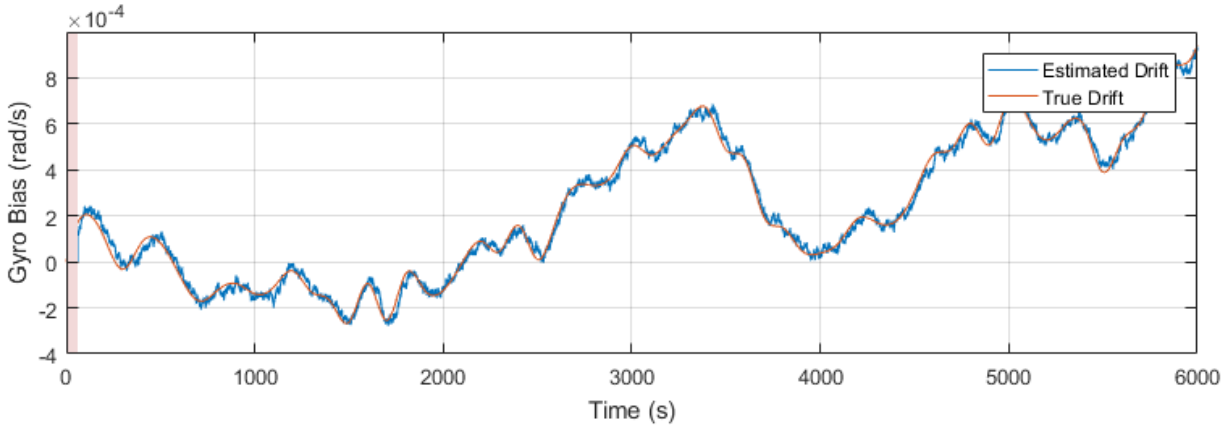

Fig. 8 The actual (red) and estimated (blue) MEMS gyroscope bias, $\mathcal{B}(t)$ and $\hat{\mathcal{B}}(t)$, over the course of a full simulated orbit.

The Root Mean Square Error (RMSE) of the bias estimate over the entire orbit is consistently held to under 3×10^{-5} rad/s with the simulated gyro and star tracker, corresponding to less than 2.5% error in the commanded rate of satellite. This also corresponds to approximately 24% of the one-period bias instability $\Delta\mathcal{B}$ of the gyroscope. Even over orbital timescales significantly longer than those of the gyro bias drift, the estimator is able to hold the bias error to fractions of the bias instability. The maximum error noted after the startup transient was typically less than 1×10^{-4} rad/s, only three times the RMSE error and equivalent to approximately 8% of the commanded satellite rate.

C. External Torque and Density Estimation

Multiple density profiles were used to test, categorized as either periodic or non-periodic. The periodic waveforms where comprised of low-frequency sinusoidal density profiles, roughly representative of the known atmospheric density variation from the light to dark side of the planet (and described in the Harris-Priester atmospheric model [3]). The non-periodic test waveform used was an unrealistic frequency chirp used to test the system's frequency response.

1. Periodic Density Profiles

The first tested density profile $\rho_1(t)$ was a high-amplitude cosine wave from 0 $\mathrm{kg/m^3}$ to 10×10^{-12} $\mathrm{kg/m^3}$ with a period equal to the orbital period, described by Equation 24. This replicates the shape of a Harris-Priester atmosphere, but with a larger amplitude than expected at 400 km. (The Harris-Priester maximum and minimum for this height are approximately 7.5×10^{-12} $\mathrm{kg/m^3}$ and 2.2×10^{-12} $\mathrm{kg/m^3}$, respectively [3].) The second profile $\rho_2(t)$ is a more complex sinusoid with higher-frequency components and a smaller amplitude, meant to test unpredictable changes in the atmosphere and higher altitudes. It is described by Equation 25, and roughly approximates the amplitude of the Harris-Priester atmospheric variation at 440 km, but with extra, higher-frequency variation.

$$\rho_1(t) = 5 \times 10^{-12}\ \mathrm{kg/m^3}\,(1 - \cos\Pi(t)) \tag{24}$$

$$\rho_2(t) = 3 \times 10^{-12}\ \mathrm{kg/m^3} - 1 \times 10^{-12}\ \mathrm{kg/m^3} \cos\Pi(t) - 5 \times 10^{-13}\ \mathrm{kg/m^3} \cos 4\Pi(t) \tag{25}$$

Under multiple tests with the first test atmosphere ρ_1, the RMS error of the external torque estimate was found to be 7.7×10^{-8} Nm, or 2.5% of the range of torques measured. The RMS error of the density estimate corresponding to these estimates was fairly consistent at around 1.3×10^{-13} $\mathrm{kg/m^3}$, or 1.3% of the density amplitude.

Under multiple tests with the second test atmosphere ρ_2, the RMS error of the external torque estimate was reduced to 3.5×10^{-8} Nm, approximately 5% of the range of torques measured. The RMS error of the density estimate corresponding to these estimates was approximately 1.0×10^{-13} $\mathrm{kg/m^3}$, or 5.0% of the density amplitude. A typical estimated external torque response to ρ_2 is shown in Fig. 9. All error values are summarized in Table 4.

2. Frequency Response

The final density waveform tested was a non-periodic frequency chirp in density, unrepresentative of actual atmospheric density variation. This was used to investigate the frequency response of the system. The waveform used, ρ_3, was a quadratic frequency chirp from 1/15 $\mathrm{min^{-1}}$ to 2 $\mathrm{min^{-1}}$, with an amplitude of 2×10^{-12} $\mathrm{kg/m^3}$. This level of variation is roughly equivalent to tracking the orbital density variation around 440 km. Figure 10 shows a Bode plot summary of the frequency response of the system to this profile.

The -3 dB bandwidth is equal to 1 $\mathrm{min^{-1}}$, which sensibly corresponds with the bandwidth of the low-pass filter used in the estimator. The phase margin at the -3 dB point is approximately 95°, showing that the system can still track high-rate changes with manageable phase lag.

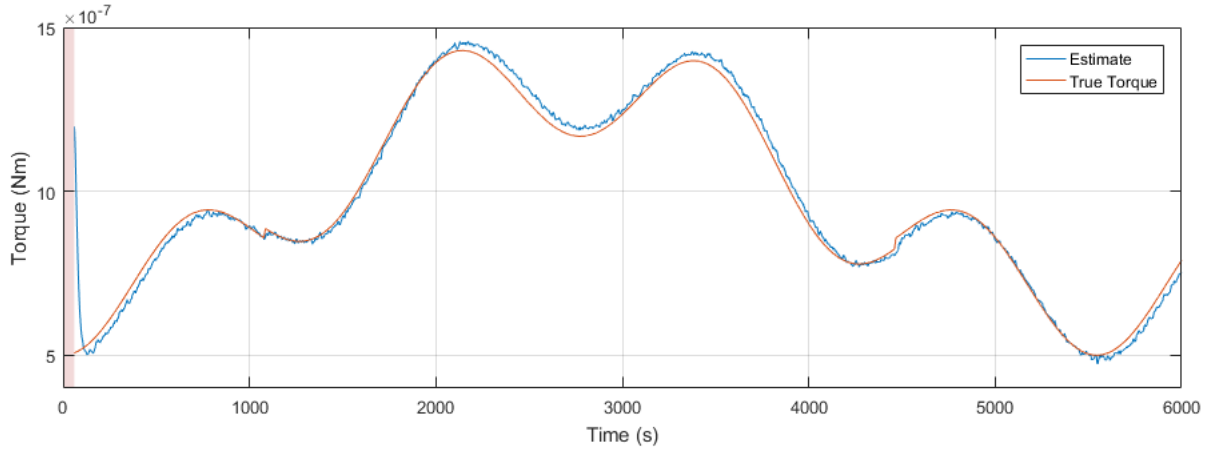

Fig. 9 System estimation of the external torque in a modeled atmosphere of the second type, ρ_2. This response is typical for the tested density waveforms. Note that slight torque discontinuities can be seen in the actual torque due to the entering and exiting of eclipse.

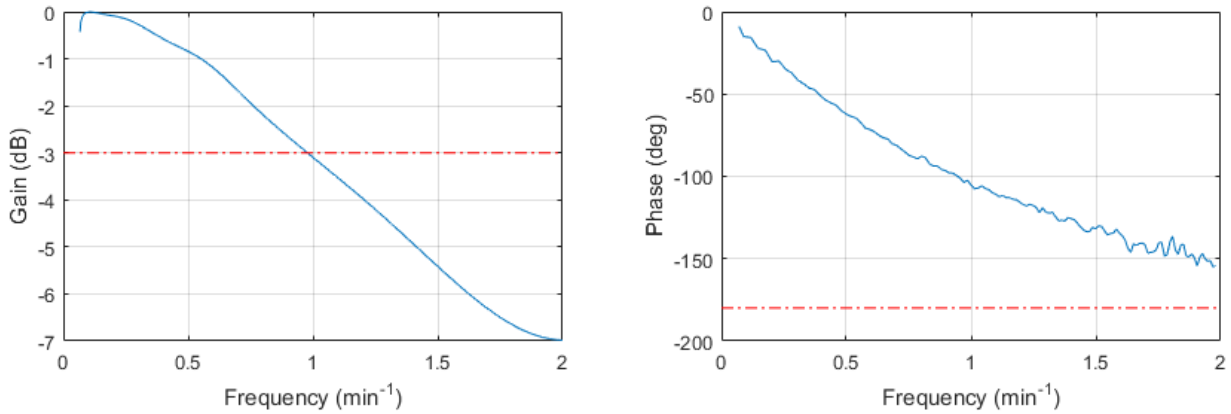

Fig. 10 Bode plot of the density estimation frequency response. Simulated using a density chirp with an amplitude of 2×10^{-12} kg/m^3.

D. Desaturation

The simulation has shown that the flipping maneuver used to desaturate the reaction wheel is effective, and can be performed without long-term upset to the external torque estimation. Figure 11 shows the output of the density estimator during a typical flipping maneuver.

It can be seen that the flipping maneuver occurring during the measurement of a periodic density waveform induces a temporary error at approximately four times the RMS error of the overall density measurement. That, combined with the fact that this anomaly occurs predictably at known times, shows that the external torque and density estimation is robust to this desaturation technique. Simulation shows that a change in desaturation mode will be required approximately every 8 hours during normal measurement operations. Since the maneuver takes two minutes, this gives the system a downtime of 0.4% of the total operational time due these flips.

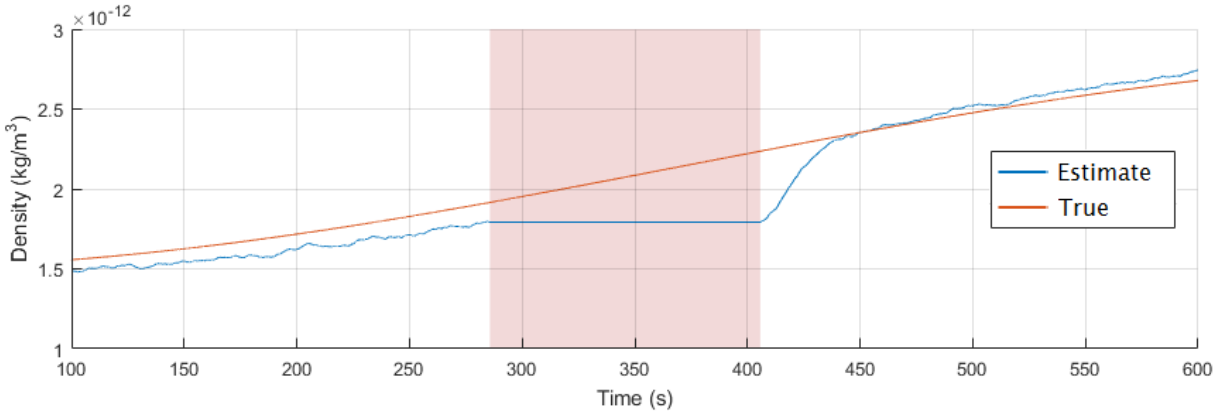

Fig. 11 The actual (red) and estimated (blue) atmospheric density during a flipping maneuver. The shaded region of the plot indicates the period of time when the estimators of torque and density are paused for the flip.

V. Global Estimation and Constellation Design

It has been shown that an individual SPATULA satellite is an effective way to measure local density. By combining these measurements, a constellation of SPATULA spacecraft can be used to produce an estimated global density map.

A. Spherical Harmonic Density Function Estimation

If it is assumed that the density is a smooth function on the surface of a sphere (the shell with radius equal to the spacecraft orbital radius), then the global density estimate can be described by a series of spherical harmonics according to equation 26.

$$\hat{\rho}(\Omega) = \sum_{\ell,m}^{\ell_{\max}} a_{\ell,m} Y_{\ell,m}(\Omega) \tag{26}$$

Here, $Y_{\ell,m}$ is used to denote the Laplace spherical harmonics of degree ℓ and order m, and $a_{\ell,m}$ is the coefficient of $Y_{\ell,m}$. The longitude λ and latitude ϕ define $\Omega = (\lambda, \phi)$, the solid angle location on the spherical shell. $\ell_{\max}$ is the maximum spherical harmonic degree of the density estimate function.

Suppose a SPATULA satellite has made many density measurements, evenly spaced in time over the course of one orbit. The vector of raw measurements $\boldsymbol{\rho}'$ can be converted to a corrected measurement vector for the orbit $\boldsymbol{\rho}^c$ using an approximate inverse of the frequency-domain transfer function depicted in Fig. 10, up to some cutoff frequency f_{cutoff} (to avoid division by arbitrarily small, poorly-characterized gains). If the estimated transfer function of the SPATULA estimator is defined by a gain term $G(f)$ and a phase term $\psi(f)$, then the vector of corrected measurements $\boldsymbol{\rho}^c$ is given by

$$\boldsymbol{\rho}^c = \text{IFFT}\left(\text{FFT}\left(\boldsymbol{\rho}'\right) \cdot \begin{cases} \frac{1}{G(f)} e^{-i\psi(f)} & \text{for } |f| < f_{\text{cutoff}} \\ 1 & \text{for } |f| \geq f_{\text{cutoff}} \end{cases}\right). \tag{27}$$

If the orbital period is P, then f_{cutoff} should be close to but greater than $\ell_{\max}/P$, since at most $\ell_{\max}$ oscillations per orbit

can be characterized by the density estimate function, equation 26.

Combining the corrected measurement vectors from each satellite, the constellation has made N corrected density measurements $\rho_1^c \dots \rho_N^c$ at locations $\Omega_1 \dots \Omega_N$. Estimating the global density function requires estimating the spherical harmonic coefficients $a_{\ell,m}$ from these measurements around the sphere. The procedure for doing this is given by Pollaine and Haan [22]. The goal is to find the coefficients that minimize the least-squares error function

$$\hat{\boldsymbol{a}} = \underset{a_{\ell,m}}{\operatorname{argmin}} \frac{1}{2} \sum_{i=1}^{N} \left(\sum_{\ell,m}^{\ell_{\max}} \left(a_{\ell,m} Y_{\ell,m} \left(\Omega_i \right) \right) - \rho_i^c \right)^2 \tag{28}$$

where $\hat{\boldsymbol{a}}$ is the estimated vector of spherical harmonic coefficients. By setting partial derivatives to zero and rearranging, this gives the set of equations

$$\sum_{p,q}^{\ell_{\max}} a_{p,q} \left(\sum_{i=1}^{N} Y_{p,q} \left(\Omega_i \right) Y_{\ell,m} \left(\Omega_i \right) \right) = \sum_{i=1}^{N} \rho_i^c Y_{\ell,m} \left(\Omega_i \right) \ . \tag{29}$$

These equations by Pollaine and Haan are equivalent to the following matrix equation:

$$\underbrace{\sum_{i=1}^{N} \begin{bmatrix} Y_{0,0}\left(\Omega_i\right) Y_{0,0}\left(\Omega_i\right) & \dots & Y_{0,0}\left(\Omega_i\right) Y_{\max}\left(\Omega_i\right) \\ Y_{1,-1}\left(\Omega_i\right) Y_{0,0}\left(\Omega_i\right) & \dots & Y_{1,-1}\left(\Omega_i\right) Y_{\max}\left(\Omega_i\right) \\ Y_{1,0}\left(\Omega_i\right) Y_{0,0}\left(\Omega_i\right) & \dots & Y_{1,0}\left(\Omega_i\right) Y_{\max}\left(\Omega_i\right) \\ Y_{1,1}\left(\Omega_i\right) Y_{0,0}\left(\Omega_i\right) & \dots & Y_{1,1}\left(\Omega_i\right) Y_{\max}\left(\Omega_i\right) \\ \vdots & \ddots & \vdots \\ Y_{\max}\left(\Omega_i\right) Y_{0,0}\left(\Omega_i\right) & \dots & Y_{\max}\left(\Omega_i\right) Y_{\max}\left(\Omega_i\right) \end{bmatrix}}_{M} \underbrace{\begin{bmatrix} a_{0,0} \\ a_{1,-1} \\ a_{1,0} \\ a_{1,1} \\ \vdots \\ a_{\max} \end{bmatrix}}_{\hat{\boldsymbol{a}}} = \underbrace{\sum_{i=1}^{N} \rho_i^c \begin{bmatrix} Y_{0,0}\left(\Omega_i\right) \\ Y_{1,-1}\left(\Omega_i\right) \\ Y_{1,0}\left(\Omega_i\right) \\ Y_{1,1}\left(\Omega_i\right) \\ \vdots \\ Y_{\max}\left(\Omega_i\right) \end{bmatrix}}_{\boldsymbol{z}} \tag{30}$$

where $Y_{\max} = Y_{\ell_{\max},\ell_{\max}}$. This can be solved by matrix inversion $\hat{\boldsymbol{a}} = M^{-1}\boldsymbol{z}$ or by a more efficient matrix left division algorithm $\hat{\boldsymbol{a}} = M \backslash \boldsymbol{z}$, as long as M is full rank. For a maximum spherical harmonic degree $\ell_{\max}$, there will be $(\ell_{\max}+1)^2$ coefficients, and so the number of measurements N must satisfy $N \geq (\ell_{\max}+1)^2$ for M to be invertible.

B. Constellation Requirements

The requirement that equation 30 be invertible establishes the absolute minimum number of observations for the estimate to be solvable; the estimate only gives meaningful results if the measurements are spread out across the surface of the sphere. Circular orbits trace great circles around a shell of constant altitude (if perturbations are ignored). For measurements made along great circle paths, Pollaine and Haan give a more stringent requirement [22]: The number of great circle paths must be at least one greater than the maximum reconstructed degree $\ell_{\max}$, and these great circles must be well-distributed over the sphere. This is certainly the more limiting requirement, since many samples can be taken around each orbit, but the number of great circles is limited by the number of constellation orbital planes.

Secondly, this only estimates the density function at one altitude. To get meaningful results throughout the upper atmosphere, it is necessary to either use outside models that can be correlated with the density at the one known altitude,

or to determine a scale height h_s. If density function estimates can be made at at least two altitudes (giving $\hat{\rho}_1(\lambda, \phi)$ at altitude h_1 and $\hat{\rho}_2(\lambda, \phi)$ at altitude h_2), then a scale height can be found and an exponential interpolation performed.

$$\hat{h}_s(\lambda, \phi) = \frac{h_2 - h_1}{\ln(\hat{\rho}_2(\lambda, \phi)) - \ln(\hat{\rho}_1(\lambda, \phi))} \tag{31}$$

$$\hat{\rho}(\lambda, \phi, h) = \hat{\rho}_1(\lambda, \phi) \exp\left(\frac{h - h_1}{\hat{h}_s(\lambda, \phi)}\right) \tag{32}$$

Lastly, consider the refresh rate of the estimate. If the atmosphere were to suddenly change, how long would it take the estimated model to completely account for it? The harmonic coefficient calculation requires samples around a great circle. If there is only one satellite per orbital plane, it will take a full orbital period P for the great circle of samples to be completely refreshed. If there are two satellites, then they can be equally spaced such that the entire great circle is re-sampled every half orbital period. Similarly, for N satellites equally spaced in a circular orbit, the entire orbit will be re-sampled and the estimation can be completely re-run at every interval P/N. New data from each satellite can be accommodated faster than this (or even as it is obtained), but the estimate function will be calculated including data as old as the complete refresh time.

From this analysis makes clear what the SPATULA constellation must look like in order to calculate an estimated spherical harmonic density map $\hat{\rho}(\lambda, \phi, h)$ with a maximum degree of $\ell_{\max}$:

- The orbit of each spacecraft should be circular (as assumed in the density estimation analysis).
- At least two constant-altitude shells should be used in order to infer a scale height.
- At least $\ell_{\max} + 1$ separate orbital planes must be used at each sampled altitude.
- The orbital planes at each altitude should be distributed to leave as few large gaps as possible.
- The number of satellites per orbital plane must be at least the orbital period divided by the desired complete refresh time of the estimate.

C. Constellation Simulation

1. Constellation Design

The ideal constellation shape for this measurement would involve orbit poles spread evenly about the Earth in a geodesic pattern. However, this would require satellites at multiple different inclinations, and the constellation would drift out of alignment due to differential nodal regression. The most critical factors in designing the constellation is to assure that the orbital planes are as spread out as possible within each orbital shell so that there are no large gaps between orbits (as this could lead to unsampled or undetermined spherical harmonic modes), and to assure that the constellation is stable. As such, Walker constellations [23] are a good starting point. If we have decided that the final constellation should be able to measure $\ell_{\max}$ spherical modes at a given altitude shell, then at least $\ell_{\max} + 1$ Walker planes is minimally sufficient.

What inclination should the planes have? The largest gap along the equator of a p-plane Walker constellation is given by

$$\Delta\text{RAAN} = \begin{cases} 360°/p & \text{if } p \text{ is even} \\ 360°/2p & \text{if } p \text{ is odd.} \end{cases} \tag{33}$$

In general, odd numbers of orbital planes are recommended for this reason. The approximate angular diameter of the polar gap is given by $180° - 2i$, where i is the inclination. This should be no larger than the equatorial plane spacing, but any smaller will increase gaps in the rest of the constellation. Therefore, i is chosen to be

$$i = \frac{1}{2}\left(180° - \Delta\text{RAAN}\right) . \tag{34}$$

The number of satellites per plane should be determined the desired estimation refresh time. Even only one per plane, with a complete refresh time on the order of 90 minutes would be sufficient for most use cases. For now, only one is considered (but more could be added flexibly at any time).

The last question is the phasing. This is not absolutely critical, but it would be good practice to choose a non-zero phasing number f such that the satellites are well-distributed; that way, the oldest samples of each great circle are not co-located. (For example, if the satellites were all phased together, then one pole would have data at least half the period old each time the estimation is run.)

The recommended configuration for a SPATULA Walker constellation is to choose an even $\ell_{\max}$, such that there are an odd number of planes. Then:

$$i = 90° \left(1 - \frac{1}{\ell_{\max} + 1}\right) , \tag{35}$$

$$t = \left\lceil \frac{P}{T_{\text{refresh}}} \right\rceil (\ell_{\max} + 1) , \tag{36}$$

$$p = \ell_{\max} + 1 , \tag{37}$$

$$f \neq 0 , \tag{38}$$

where $i : t/p/f$ describes a Walker constellation with inclination i, p planes, t total satellites, and a phasing number f. At least two of these constellations, at different altitudes, must be established. An example configuration of two nested 84°: 15/15/1 constellations is shown in Fig. 12.

2. Simulation

Previous atmospheric models have used a relatively low maximum harmonic degree due to lack of observable test satellites. (For example, the Air Force High Accuracy Satellite Drag Model, or HASDM [24], uses $\ell_{\max} = 2$.) This constellation would enable much higher orders; as a proof of concept, $\ell_{\max} = 14$ was chosen, although this is by no means a limit.

Two SPATULA Walker 84°: 15/15/1 constellations were simulated using Matlab, at 400 km and 500 km altitude, as

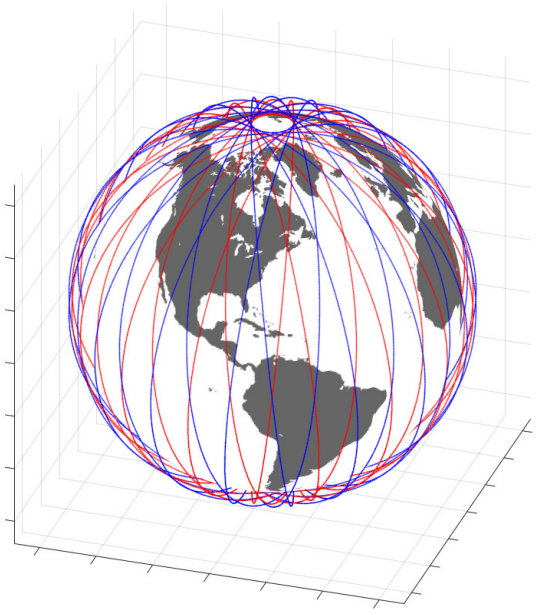

Fig. 12 Nested 84°: 15/15/1 Walker constellations used for constellation simulation.

shown in Fig. 12. Non-physical high-order test atmospheres of degree $\ell_{\max} = 14$ were randomly generated at each altitude, within the bounds specified by the Harris-Priester model [3]. To simulate the density measurements, the actual density was sampled once per minute around the orbit, and was put through a transfer function based on that shown in Fig. 10. In each case, the transfer function was calculated by randomly generating a curve within a 20% envelope (3σ) around the actual transfer function curve. Then, the data was corrected according to equation 27 using the original Fig. 10 transfer function curve and a cutoff frequency of $2\ell_{\max}/P$. (This replicates correction using an imperfect characterization of the satellites.) The corrected measurements were then used to estimate the atmosphere parameters by the inversion of equation 30 using an efficient matrix left division algorithm. Typical simulation results are shown in figures 13 through 15.

The density estimates have errors less than 1% of the maximum density observed at each altitude. The peaks in estimation error, as expected, fall in the largest gaps of the Walker constellation. The scale heights show small isolated spots of larger errors, but still within a few kilometers of the correct value. The great majority of the map, outside of these small zones, is within a kilometer or so of the correct value, again approximately a 1% error. Clearly, even with imperfect transfer function characterization this constellation is able to sample and estimate the spherical harmonic coefficients up to degree 14. This yields a $15^2 = 225$ -parameter model in each shell, and a 450-parameter model overall, which is a vast improvement over current empirical models. And again, remember that these atmospheres are non-physical: They have high-order content not likely to be seen in a real atmosphere, where the effects of these spot errors will likely by lessened.

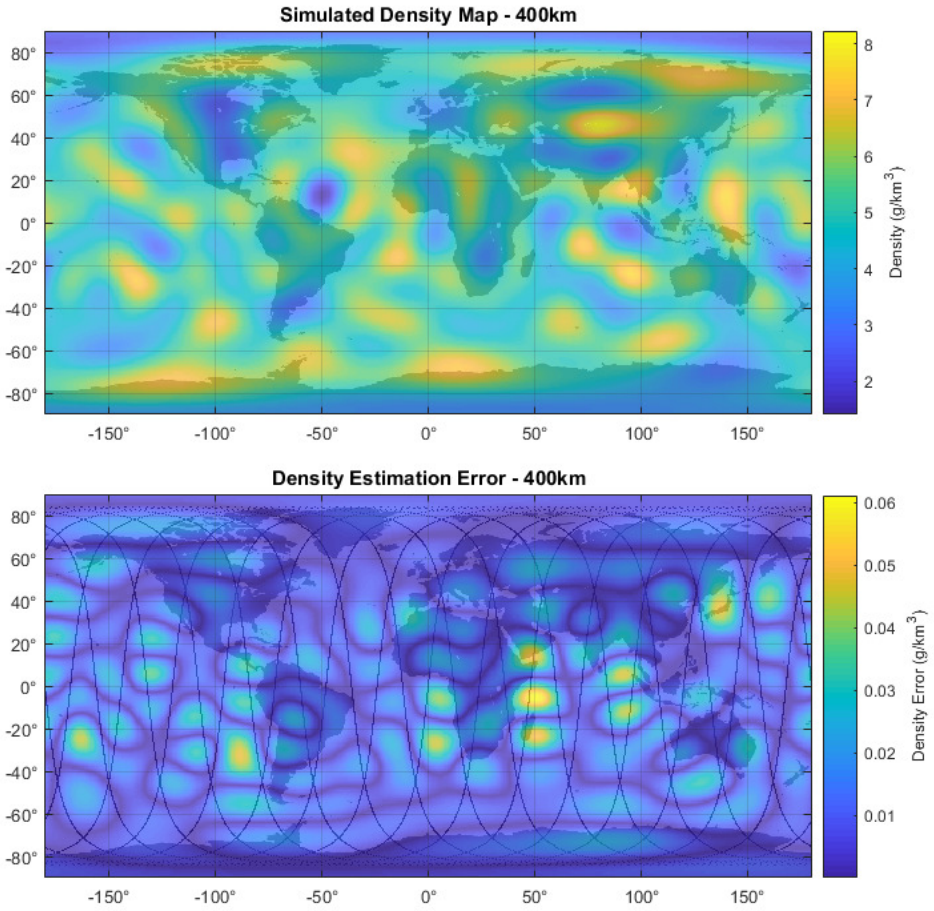

Fig. 13 Simulated density map and estimation error at 400 km altitude

VI. Conclusion

A. Summary of Results

Table 4 list a summary of the key estimation error parameters discovered through simulation and discussed in the previous sections.

It can be seen that this initial analysis validates SPATULA as a solution to the stated problem: SPATULA can provide density measurement capability with accuracy and frequency on par with other available methods, but to do so in a cubesat form factor using commercially-available sensors. The stand-alone SPATULA system is able track density variation using on-board real-time estimators, with a bandwidth high enough to track quick, minute-scale variations. The bandwidth is comparable to other proposed density-measuring small satellites [5], despite being approximately 50 times smaller. Without the use of specially designed ultra-high-precision science instruments, SPATULA is able to provide results roughly replicating those of the CHAMP and GRACE dedicated science satellites, but do so with no ground-based post processing. Assuming the approximate 1×10^{-13} kg/m^3 RMS error is preserved, this means that the satellite should be able to provide useful drag estimates from the low 300 km altitude orbits into the domain of

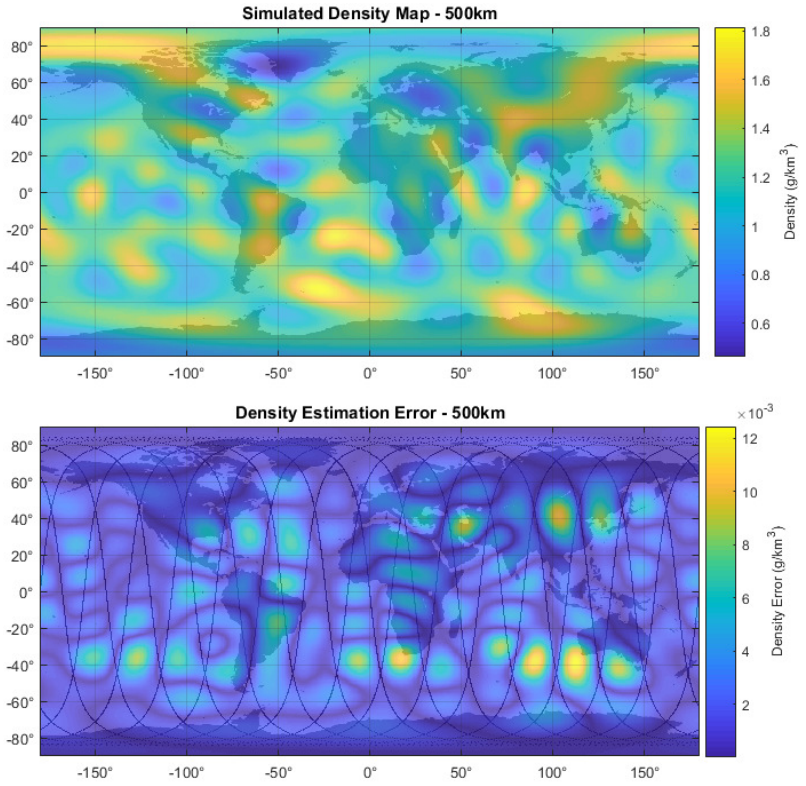

Fig. 14 Simulated density map and estimation error at 500 km altitude

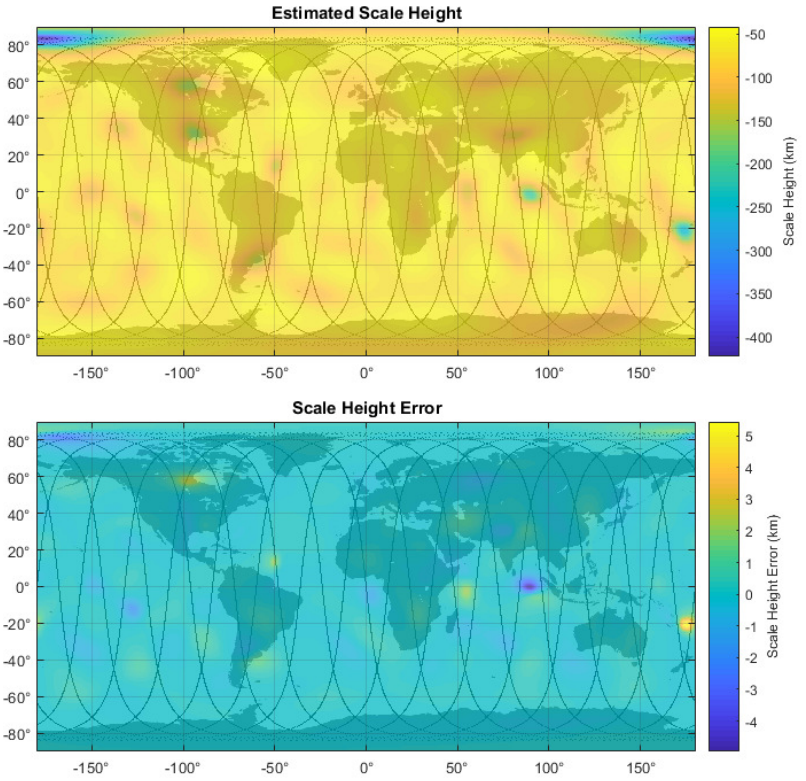

Fig. 15 Estimated scale height and estimation error

Table 4 Major Results and Estimation Errors

Error Subject	Error Type	Value	Notes
Satellite Moment of Inertia	Relative	0.02% J_{sat}	Limited by RW noise
Reaction Wheel MOI	Relative	$< 1 \times 10^{-6}$ J_{rw}	—
Gyroscope Bias Estimate	RMSE	$< 3 \times 10^{-5}$ rad/s	< 25% $\Delta\mathcal{B}$
	Maximum	$< 1 \times 10^{-4}$ rad/s	—
ρ_1 τ_{ex} Estimation Error	RMSE	7.7×10^{-8} Nm	—
	Relative	2.5% τ_{ex} Amplitude	—
ρ_1 Estimation Error	RMSE	1.3×10^{-13} kg/m^3	$\sim$ ρ variation at 740 km
	Relative	1.3% ρ_1 Amplitude	—
ρ_2 τ_{ex} Estimation Error	RMSE	3.5×10^{-8} Nm	—
	Relative	5.0% τ_{ex} Amplitude	—
ρ_2 Estimation Error	RMSE	1.0×10^{-13} kg/m^3	$\sim$ ρ variation at 740 km
	Relative	5.0% ρ_2 Amplitude	—
Desaturation Flip Downtime	Absolute	120 s/flip	—
	Relative	0.4% operation	—
Desaturation Flip $\hat{\rho}$ Error	Relative	4 RMSE($\hat{\rho}$)	During known time
-3 dB $\hat{\rho}$ Estimation Bandwidth	Absolute	1 min^{-1}	Above 90 orbit^{-1}
-3 dB Point Phase Margin	Absolute	95°	—
Optimal Walker constellation configuration:		$\ell_{\max}$ is even	—
		$i = 90° \left(1 - \frac{1}{\ell_{\max}+1}\right)$	—
		$t = \left\lceil \frac{P}{T_{\text{refresh}}} \right\rceil (\ell_{\max} + 1)$	—
		$p = \ell_{\max} + 1$	—
		$f \neq 0$	—
Density test map reconstruction error:		$O\,(1\%)$	With 20% 3σ TF error

sun-synchronous orbits in the >600 km altitude range. The bandwidth is high enough to capture quick transients near the poles, as well as sudden changes due to solar activity, and the accuracy is high enough to provide meaningful input for the creation of new thermospheric models.

Since it is small, and uses commercial-grade measurement equipment, it can be made inexpensive enough to enable a measurement constellation able to provide a near-real-time spherical harmonic global density map. This constellation can be made to operate up to high spherical harmonic degrees, but does not require them in order to yield valuable maps: The constellation can be gracefully deployed, slowly adding orbital planes and increasing the estimated harmonic degree until the full constellation is set up. Once the desired maximum degree is achieved, more satellites can be added to each orbital plane in order to decrease the complete refresh time of the estimation. The independence of each satellite, and the global nature of the estimation, means that no one satellite or subset is critical to the operation of the constellation; simply decreasing the estimated degree can account for any satellite loss. This property makes a SPATULA constellation an attractive project for investment — increasing return can be seen with each added satellite,

and the risk of constellation failure is very low.

The SPATULA drag arm technique provides a way to multiply the measured quantity (torque), without sacrificing performance or lifetime of the spacecraft. Compare this technique to increasing the drag area, which would allow the multiplication of drag force to enable measurement with less expensive accelerometers, but would come at the expense of lifetime due to the decreased ballistic coefficient. Measuring drag forces through their torque effects, then, has been shown to be a valid approach to the density-estimation problem. Since so many of the perturbing orbital forces induce no appreciable torques, the toque domain provides a much cleaner measurement to the estimator, and enables density measurement with less expensive sensors and less knowledge of external forces.

B. Limitations of the Measurement Method

This analysis assumes perfect knowledge of the constant coefficient of drag, an unrealistic prospect. The coefficient of drag is unpredictable, and can change over time due to solar activity, temperature, and light conditions [13]. With no measurement of the C_D, the same methodology estimates the product of the drag coefficient and the atmospheric density. This is a flaw common to all systems that aim to measure density through the drag force, however, and in the end the $\rho \cdot C_D$ product is the parameter necessary to predict orbital motion. Even a perfect measurement of density would not allow perfect prediction of orbital motion, since this uncertainty in the coefficient of drag is equally a problem for the satellite subject to prediction. In the end, the estimation of the $\rho \cdot C_D$ product is sufficient to qualify the success of this analysis.

Secondly, the torque measurements herein prove ineffective at measuring cross-path velocities and forces. By the nature of the drag arm setup, the satellite is only sensitive to along-track velocity relative to the atmosphere. While a highly-calibrated accelerometer like those of the CHAMP and GRACE spacecraft are able to roughly measure the cross-track orbital winds [6] - [8], this system is not sensitive to non-ram velocities. Adding a second drag arm along the z axis of the satellite could provide some information, but the measurements would be coupled to those about the main axis by rotational dynamics, and the sensitivity would be greatly reduced without orbital ram velocities to increase the drag force. While this means that those uncertainties will not taint the measurement, it does mean that more SPATULA satellites, in different orbital planes, are necessary to quantify the full vector nature of the thermospheric winds.

C. Limitations of the Study, and Future Work

The next steps involve increasing the fidelity of disturbances included in the model. First, a consideration of residual magnetic moment of the craft must be made (as it was assumed zero in this analysis). The typical order of this effect is quite small, as can be seen in Fig. 1, but it must eventually be accounted for. These torques are observable, however, and can be estimated to negate their effect on the measurement. Furthermore, the self-desaturating nature of the proposed system means that magnetorquers will only be needed to desaturate the non-measurement axes. Additionally,

self-shadowing effects should be incorporated by using a more advanced SRP model [25], and emitted IR torques should be examined, or thermal studies should be done to justify neglecting them.

Uncertainties in spacecraft parameters which were assumed constant should also be injected into future simulations; these errors can then be estimated on orbit, or calibrated based on some external reference data. Most of parameters can be fairly well-characterized on Earth (e.g. spacecraft physical dimensions and thermal deformations), but those properties which are more uncertain (e.g. reflection coefficients) will increase density measurement noise. However, the order of these effects should be relatively small; for example, the discontinuities in the true torque curve of Figure 9 show that the magnitude of SRP effects are an order of magnitude smaller than those due to drag, so even relatively large uncertainties will not dominate the measurement error observed in this study.

Additionally, the model of the reaction wheel must be augmented to include reaction wheel jitter and control noise. The current model includes the finite bandwidth of the commanded torque, but assumes that the wheel can produce an accurate and smooth torque when the command is constant. This could in theory be corrected by extensive testing and tweaking of the reaction wheel internal torque controller to account for internal variation, but this must be modeled.

Lastly, the simulation should be brought from the present 3-DoF model into a full 6-DoF model that accounts for cross-axis effects and non-linearities. This model is certainly sufficient to demonstrate that the SPATULA concept enables realistic, commercially-available sensors to measure atmospheric density in LEO, but the controller and state estimator will need to be re-worked to be compatible with a fully 3-axis-stabilized spacecraft.

Appendix

Force and Torque Models

The attitude and position response of the SPATULA spacecraft was simulated under the influence of atmospheric drag, solar radiation pressure, and gravity.

1. Atmospheric Drag

Atmospheric drag is modeled separately on each surface of the spacecraft, according to

$$\mathbf{F}_D = \sum_{i=1}^{N_{\text{surf}}} \mathbf{F}_{D,i} = -\sum_{i=1}^{N_{\text{surf}}} \frac{1}{2}\rho v^2 C_D A_i \cos\alpha_i \hat{\mathbf{v}} \tag{39}$$

where α_i is the angle between the surface normal and the velocity vector of the spacecraft. The coefficient of drag, C_D, is considered constant at 2.2 for all surfaces, which is a typical value used for satellites in low orbit [26]. The combined action of these forces produces an aerodynamic torque given by

$$\tau_D = \sum_{i=1}^{N_{\text{surf}}} \mathbf{r}_{cm-i} \times \mathbf{F}_{D,i} \tag{40}$$

where $\mathbf{r}_{cm-i}$ is the vector from the spacecraft center of mass to the centroid of surface i.

2. Solar Radiation Pressure

The radiation pressure conditions on each surface of the spacecraft can be described by the coefficient of specular reflection η_s, the coefficient of diffuse reflection η_d, and the coefficient of absorption η_a. Specifying any two of these values is sufficient to solve for the third via Equation 41, which accounts for the conservation of the reflected and absorbed energy.

$$\eta_s + \eta_d + \eta_a = 1 \tag{41}$$

For this simulation, these values were given moderate values of 0.3, 0.3, and 0.4, respectively, corresponding to a semi-reflective/diffuse material with an absorptivity similar to a light (but not white) paint. Given these coefficients for each surface, and assuming that the surfaces have uniform properties, the solar radiation pressure force on each unshaded surface is given in terms of the unit vector normal to the surface $\hat{\mathbf{N}}_i$ and the unit vector toward the sun $\hat{\mathbf{S}}$ as

$$\mathbf{F}_{s,i} = -2\frac{W}{c}A_i\eta_{s,i}\cos^2\gamma_i\,\hat{\mathbf{N}}_i \tag{42}$$

$$\mathbf{F}_{d,i} = \frac{W}{c}A_i\eta_{d,i}\left(-\frac{2}{3}\cos\gamma_i\,\hat{\mathbf{N}}_i - \cos\gamma_i\,\hat{\mathbf{S}}\right) \tag{43}$$

$$\mathbf{F}_{a,i} = -\frac{W}{c}A_i\eta_{a,i}\cos\gamma_i\,\hat{\mathbf{S}} \tag{44}$$

$$\mathbf{F}_{SRP} = \sum_{i=1}^{N_{\text{surf}}}\mathbf{F}_{SRP,i} = \sum_{i=1}^{N_{\text{surf}}}\left(\mathbf{F}_{s,i} + \mathbf{F}_{d,i} + \mathbf{F}_{a,i}\right) \tag{45}$$

where c is the speed of light, γ_i is the angle between the surface normal and the incoming sunlight, and A_i is the area of the considered surface [27]. The solar constant W is considered to be 1361 $\mathrm{W/m^2}$ outside of Earth eclipse, zero inside the umbra of Earth's shadow, and vary linearly between these two values as the spacecraft passes through the penumbra. The total force on the spacecraft is given by the sum of these forces on each of the N non-shaded surfaces, and the torque is

$$\tau_{SRP} = -\sum_{i=1}^{N_{\text{surf}}}\mathbf{r}_{cm-i}\times\mathbf{F}_{SRP,i} \tag{46}$$

where $\mathbf{r}_{cm-i}$ is the vector from the spacecraft center of mass to the centroid of surface i.

3. Gravity and Gravity Gradient

Gravity is modeled as Newtonian gravity from a spherical Earth, acting separately at the center of mass of each major component of the spacecraft.

$$\mathbf{F}_g = \sum_{i=1}^{N_{\text{comp}}}\mathbf{F}_g = -\mu_\oplus\sum_{i=1}^{N_{\text{comp}}}\frac{m_i}{r_i^3}\mathbf{r}_i \tag{47}$$

The vector $\mathbf{r}_i$ gives the location of the component's center of mass relative to the center of the Earth, and r_i gives the magnitude of this vector. Except for the extended boom, all components are of small aspect ratio. The boom itself is

a small fraction of the spacecraft mass. Thus, the spacecraft is very well approximated by an extended collection of rigidly-connected point masses (i.e. a "dumbbell" model), and the gravity gradient torque is implicitly modeled by the force of gravity acting separately at each center of mass.

$$\tau_g = \sum_{i=1}^{N_{\text{comp}}} \mathbf{r}_{cm-i} \times \mathbf{F}_{g,i} \tag{48}$$

Sensor and Actuator Models

The SPATULA spacecraft as simulated has five main sensors and one main actuator: A star tracker, an Earth horizon sensor, a MEMS gyroscope, a GPS receiver, and a reaction wheel with rate readout. These provide the only information input to the control and estimation systems of the spacecraft. The noise characteristics of these signals are listed in Table 2.

4. Attitude Sensors

The star tracker and the Earth horizon sensors are both modeled as discrete-time signals with zero-mean Gaussian noise and quantized output. At each sample $n = 0, 1, 2\ldots$ both sensors give a measured angle $\theta'[n]$ according to

$$\theta'[n] = \Delta \left\lfloor \frac{\theta(n/f_s) + V_n}{\Delta} \right\rceil \tag{49}$$

$$V_n \sim \mathcal{N}(0, \sigma^2) \tag{50}$$

where Δ is the resolution of quantization, f_s is the sample rate in Hz, and σ is the standard deviation of the noise. The notation $\lfloor \cdot \rceil$ represents rounding to the nearest integer. The values of these constants for each sensor are given in Table 2.

5. MEMS Gyroscope

The MEMS Gyroscope is modeled as a discrete-time signal with zero-mean Gaussian noise, quantized output, and a continuously-drifting zero-rate bias $\mathcal{B}(t)$.

$$\dot{\theta}'[n] = \Delta \left\lfloor \frac{\theta(n/f_s) + \mathcal{B}(n/f_s) + V_n}{\Delta} \right\rceil \tag{51}$$

$$V_n \sim \mathcal{N}(0, \sigma_{gy}^2) \tag{52}$$

The noise deviation, quantization resolution, and sample rate are given in Table 2. The Angular Random Walk (ARW) of the gyroscope for the given noise and sampling parameters is $ARW = \sigma_{gy}/\sqrt{f_s} \approx 0.36°/\sqrt{\text{hr}}$. The bias is a continuous random signal, generated before a run of the simulation according to the following method: Assume the startup behavior of the gyroscope is well-characterized, and therefore the bias can be calibrated to 0 at time $t = 0$. Given the gyroscope

bias instability $\Delta\mathcal{B} = 0.0072°/\text{s}$ [17], generate a random walk of Gaussian random variables by

$$\mathcal{B}_0 = 0 \tag{53}$$

$$\mathcal{B}_n \sim \mathcal{N}(\mathcal{B}_{n-1}, \Delta\mathcal{B}^2) \tag{54}$$

Lastly, assuming that the bias instability was measured with a typical minimum Allan variance period of about 100 s [28], use cubic spline interpolation to generate a continuous-time bias signal $\mathcal{B}(t)$ such that the various values of $\mathcal{B}_n$ occur at times $t_n = (100n)\,\text{s}$.

6. Reaction Wheel

Though a 3-axis-stabilized satellite requires three non-redundant reaction wheels, only one is modeled in this simulation. It is assumed that the other two are small and have negligible effect on the measurement axis of the craft, because the spacecraft is designed to maximize the effects of disturbance torques around the considered rotation axis and minimize those around others. The modeled reaction wheel is based on the Sinclair Interplanetary RW-0.01 reaction wheel [19], a small reaction wheel with on-orbit operational experience in smaller cubesats. The wheel takes in a torque command τ_c, and has finite-bandwidth dynamics modeled by

$$\dot{\tau}_{rw} = k_{rw}(\tau_c - \tau_{rw}) \tag{55}$$

$$k_{rw} = (2\pi b_{rw})^{-1} \tag{56}$$

where τ_{rw} is the current torque provided by the reaction wheels and b_{rw} is the control bandwidth of the reaction wheels, set at 100 Hz for this model. The reaction wheel outputs a rate measurement ω'_{rw} as a discrete-time signal with zero-mean Gaussian noise and quantized output governed by

$$\omega'_{rw}[n] = \Delta \left\lfloor \frac{\omega_{rw}(n/f_s) + V_n}{\Delta} \right\rfloor \tag{57}$$

$$V_n \sim \mathcal{N}(0, \sigma^2_{rw}) \tag{58}$$

7. GPS Receiver

The GPS receiver is modeled as a discrete-time signal with zero-mean Gaussian noise and a quantized output. It outputs a sequence of four-dimensional data, corresponding to a 2-D position in the plane of the orbit, $\mathbf{r}$, and a 2-D velocity in the plane of the orbit, $\mathbf{v}$.

$$\begin{bmatrix} \mathbf{r}'_{gps} \\ \mathbf{v}'_{gps} \end{bmatrix}[n] = \Delta \left\lfloor \frac{[\mathbf{r}(n/f_s)\ \mathbf{v}(n/f_s)]^T + \mathbf{V}_n}{\Delta} \right\rfloor \tag{59}$$

$$\mathbf{V}_n \sim \mathcal{N}(0_{4,1}, [\sigma^2_{gps}\ \sigma^2_{gps}\ \sigma^2_{gpsv}\ \sigma^2_{gpsv}]^T) \tag{60}$$

References

[1] Henry, C., "SpaceX, OneWeb Detail Constellation Plans to Congress," *Space News*, October 26, 2017. URL: `http://spacenews.com/spacex-oneweb-detail-constellation-plans-to-congress/` [cited 1 November 2017].

[2] Vallado, D. A. , "An Analysis of State Vector Propagation Using Differing Flight Dynamics Programs," *AAS/AIAA Space Flight Mechanics conference at Copper Mountain, CO*, January 2005. AAS 05-199 Rev 2.

[3] Harris, I. and Priester, W., "Atmospheric Structure and Its Variation in the Region from 120 to 800 Km," *COSPAR International Reference Atmosphere (CIRA) 1965*, Space Research IV, North Holland Publishing Co., Amsterdam.

[4] Koehler, C., Jasper, L., and Kemble, K., "Drag and Atmospheric Neutral Density Explorer (DANDE)," AFRL-SR-AR-TR-09-0272.

[5] Pilinski, M. D. and Palo, S. E., "An Innovative Method for Measuring Drag on Small Satellites," 23^{rd} *Annual AIAA/USU Conference on Small Satellites*.

[6] Bruinsma, S., Tamagnan, D., and Biancale, R., "Atmospheric Densities Derived from CHAMP/STAR Accelerometer Observations," *Planetary and Space Science*, Vol. 52, 2004, pp. 297-312.

[7] von Engeln, A., Teixeira, J., Wickert, J., and Buehler, S. A., "Using CHAMP Radio Occultation Data to Determine the Top Altitude of the Planetary Boundary Layer," *Geophysics Research Letter*, Vol. 32, No. 6, L06815. doi: 10.1029.

[8] Tapley, B. D., Ries, J. C., Bettadpur, S., and Cheng, M., "Neutral Density Measurements from the Gravity Recovery and Climate Experiment Accelerometers," *Journal of Spacecraft and Rockets*, Vol. 44, No. 6, Nov-Dec 2007, pp. 1220-1225. doi: 10.2514/1.28843.

[9] Tighe, A. P., Iwanovsky, B., van Eesbeek, M., and Duzellier, S., "On-Orbit Measurement of the Columbus Lab Vacuum Environment Using the MEDET Pressure Gauge."

[10] Young, J. L., "Determination of Atmospheric Density in Low-Earth Orbit Using GPS Data," *U.S.N.A. Trident Scholar project report*, No. 287, 2001.

[11] Hinks, J. C. and Piaki, M. L., "Simultaneous Orbit and Atmospheric Density Estimation for a Satellite Constellation," *AIAA Guidance, Navigation, and Control Conference*, 2-5 August 2010. AIAA 2010-8258.

[12] Mazarico, E., "A Study of the Martian Upper Atmosphere using Radio Tracking Data," *Doctoral Thesis, Massachusetts Institute of Technology*, Feb. 2008.

[13] Bowman, B. R. and Moe, K., "Drag Coefficient Variability at 175-500 km from the Orbit Decay Analyses of Spheres."

[14] Shoemaker, M. A., Wohlberg, B. E., and Koller, J., "Atmospheric Density Reconstruction Using Satellite Orbit Tomography," *AAS/AIAA Space Flight Mechanics Meeting*, April 29, 2013, Rev. 2. LA-UR-13-20735.

[15] TY-Space Ltd., "Nano Star Tracker NST-1," NST-1 datasheet.

[16] Maryland Aerospace, “MAI-SES,” MAI-SES datasheet.

[17] Analog Devices, “Low Profile Six Degree of Freedom Inertial Sensor,” ADIS16334 datasheet, 2013.

[18] SkyFox Labs, “Space-Friendly Ultra Low Power CubeSat GPS Receiver,” piNAV-L1 datasheet, Rev. H, 2017.

[19] Sinclair Interplanetary, “Picosatellite Reaction Wheels,” RW-0.01 datasheet.

[20] Norman, M.C., Peckt, M.A., and O’Shaughnessy, D.J., “In-Orbit Estimation of Inertia and Momentum-Actuator Alignment Parameters,” *AIAA Journal of Guidance, Control, and Dynamics,* vol. 34, no. 6, Nov. 2011, pp. 1798-1814.

[21] Bryson, A. E., Jr. and Ho, Y. C., “Applied Optimal Control: Optimization, Estimation, and Control.” Waltham, MA: Blaisdell, 1969. Stanford Univ., Stanford, CA and Harvard Univ., Cambridge, MA.

[22] Pollaine, S. and Haan, S. W., “Measuring Spherical Harmonic Coefficients on a Sphere.” United States. doi:. https://www.osti.gov/servlets/purl/15003912.

[23] Walker, J. G., “Satellite Constellations.” *Journal of the British Interplanetary Society*, Vol. 37, Dec 1984, pp. 559-572.

[24] Bowman, B. R. and Storz, M. F., “High Accuracy Satellite Drag Model (HASDM) Review.” *AAS/AIAA Astrodynamics Specialist Conference*, Aug. 2003. AAS 03-625.

[25] Ziebart, M., “Generalized Analytical Solar Radiation Pressure Modeling Algorithm for Spacecraft of Complex Shape,” *AIAA Journal of Spacecraft and Rockets,* vol. 41, no. 5, 2004, pp. 840-848.

[26] Oltrogge, D. L. and Leveque, K., “An Evaluation of Cubesat Orbital Decay,” 25^{th} *Annual AIAA/USU Conference on Small Satellites*, SSC11-VII-2.

[27] Wertz, J. R. et al., “Spacecraft Attitude Determination and Control,” *Astrophysics and Space Science Library*, Vol. 73. pp. 571-573. Kluwer Academic Publishers.

[28] Woodman, O. J., “An Introduction to Inertial Navigation,” *University of Cambridge Computer Laboratory*, Technical Report Number 696, p. 12.